UNIVERSITY OF NOVA GORICA

SCHOOL OF APPLIED SCIENCES

ANGULAR RESOVLED PHOTOEMISSION SPECTROSCOPY CHARACTERIZATION OF METALLIC NANOSTRUCTURED MATERIAL

DIPLOMA THESIS

Blaž Winkler

Mentor: doc. Dr. Sandra Gardonio

Nova Gorica, 2012

UNIVERZA V NOVI GORICI

FAKULTETA ZA APLIKATIVNO NARAVOSLOVJE

KARAKTERIZACIJA KOVINSKIH NANOSTRUKTURIRANIH MATERIALOV Z KOTNO ODVISNO ELEKTRONSKO SPEKTROSKOPIJO

DIPLOMSKO DELO

Blaž Winkler

Mentor: doc. Dr. Sandra Gardonio

Nova Gorica, 2012

Acknowledgement

I would like to express my greatest gratitude to doc. Dr. Sandra Gardonio for all her help and guidance during the making of this diploma thesis. I am very grateful to dr. Carlo Carbone, dr. Paolo Moras and dr Alessandro Varvaro of the Istituto di Struttura della Materia (ISM) of CNR- Italy for giving me the opportunity to participate in the beamtime at the VUV beamline at Elettra Synchrotron Laboratory where I did my experimental work presented in this thesis. I profited strongly from their close supervision and their knowledge in the field of metallic thin films and photoemission spectroscopy. I also thank the other member of the ISM-CNR group: Dr. Polina Sheverdyaeva and Dr. Alessandro Barla for their assistance during experiment and all the provided help. I thank Dr. Carlo Spezzani for his supervision during my Erasmus Training program at Sincrotrone Trieste S.C.p.A.

I also thank my family and friends for their unconditional support during the study.

Abstract

By performing photoelectron spectroscopy measurements we investigated the growth and electronic properties of FePt thin films grown on the Rh (100) surface. The FePt alloy in the $L1_0$ face-centered tetragonal (fct) phase is a potential candidate for applications in electronics due to its high magnetocrystalline anisotropy constant (perpendicular magnetic recording). A factor that limits the quality of FePt $L1_0$ thin films is the high temperature required to promote the formation of the fct phase at the expense of the parent face centered cubic phase. In this thesis we present the results of experimental investigations intended to improve the growth procedure of high quality FePt $L1_0$ thin films. High purity Fe and Pt sources were used to deposit thin FePt film on the Rh (100) surface. Nearly equiatomic FePt films were grown by alternating deposition of Fe and Pt layers in order to favor the formation of the $L1_0$ phase at relatively low temperature (380˚C). The alloy formation was monitored by measuring the Fe and Pt core levels. The electronic band structure of the FePt film surface is investigated by synchrotron radiation based angle resolved photoemission spectroscopy.

Key words: FePt $L1_0$ alloy, thin film, photoemission spectroscopy, core level, valence band.

Povzetek

Z metodo fotoelektronske spektroskopije smo raziskovali rast in električne lastnosti tankih plasti FePt zlitine na Rh (100) podlagi. FePt zlitina z ploskovno centrirano osnovno celico (faza $L1_0$) je obetaven kandidat za uporabo v elektroniki zaradi visoke magnetne anizotropije (magnetno shranjevanje podatkov). Enega večjih problemov predstavlja visoka temperatura, ki pospešuje nastajanje zlitine vendar zmanjšuje urejenost kristalne strukture. V diplomski nalogi so predstavljeni rezultati raziskave namenjeni izboljšavi metode pridobivanja visoko kvalitetne FePt zlitine. Enakomerne, izmenične plasti zelo čistega železa in platine smo naparevali na rodijevo (100) površino in z segrevanjem na relativno nizki temperaturi, 380°C, dosegli formacijo želene zlitine. Rast smo opazovali z merjenjem Fe in Pt elektronskih orbital. Elektronska stanja FePt zlitine smo raziskovali z kotno odvisno elektronsko spektroskopijo na sinhrotronsko svetlobo.

CONTENTS

LIST OF TABLES

LIST OF FIGURES

1. Introduction

1.1. $L1_0$ ordered FePt alloy

Among thin film and super lattice systems exhibiting perpendicular magnetic anisotropy, the face centered tetragonal (fct) phases of binary alloys like CoPt, FePd, and FePt, also referred to as CuAu (I) or $L1_0$ phases, have attracted much interest in recent years both from the fundamental and technological point of view. In particular, the magnetic properties of thin FePt alloy films, such as high coercivity, high saturation magnetization and large perpendicular anisotropy, open new perspectives for storage device miniaturization.

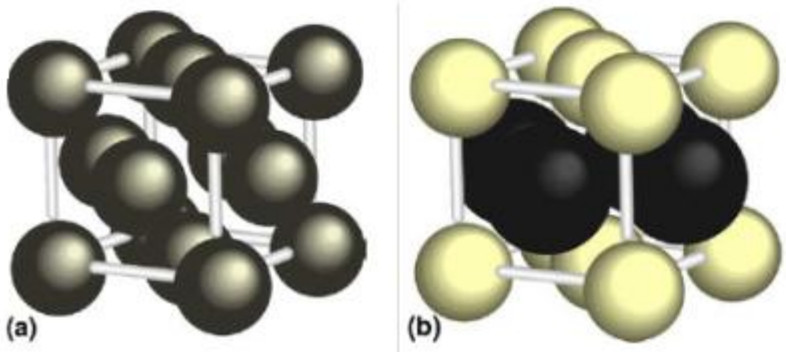

Figure 1.1 (a) fcc unit cell. (b) L10 structure showing the alternate stacking of (001) planes along the vertical axis.

The face-centered cubic (fcc) and $L1_0$ (fct) structures are shown in Fig.1.1. The fcc structure has all sites occupied by the same atoms. In the case of an alloy, the probability of each site being occupied by a specific type of atom is the same. This introduces in the structure some degree of disorder. $L1_0$ is a crystallographic derivative structure of the fcc structure. This phase can be described as a sequence of monatomic planes of the two elements Derivative structures are ordered variants of a parent structure and are usually low temperature phases, since their configuration entropy is lower that of the disordered fcc alloy parent phase. Due to the presence of different, although highly ordered, atomic species, the symmetry of the structure is lower than the parent system.

When grown with the monatomic layers parallel to the film plane, i.e., with the c-axis of the fct unit cell parallel to the film normal direction, this structure displays perpendicular magnetic anisotropy. Fully ordered FePt is predicted to have one of the largest magnetic anisotropy energies (1.6 × 10^8 erg/cm^3) [1]. Anisotropy energies > 10^8 erg/cm^3 have been found experimentally in FePt films grown by molecular beam epitaxy (MBE) [2]. These materials are attractive candidates for media applications in magneto-optical recording. The magnetic properties of FePt are deeply correlated to the structural properties of the material, i.e., the crystallographic orientation of the film, the degree of chemical ordering, and the degree of epitaxy.

1.2 Growth of FePt film on metal surface.

Epitaxial growth of chemically ordered FePt thin films with the c-axis perpendicular to the film plane by MBE [2] and by magnetron sputtering [3] was previously demonstrated. The observation of long-range chemical ordering at temperatures near 500 °C was attributed to an enhanced surface diffusion during thin film growth.

All these films were grown on dielectric MgO substrates at high temperature annealing, which tends to degrade the [001] texture of single layered FePt films and causes the grains to coarsen forming large particles.

From the point of view of magneto-electronics applications [4], the combination of metallic ferromagnets with semiconductors/metallic substrate is preferable. Moreover, from the fundamental point of view, the *in-situ* fabrication of an epitaxial film of FePt on a metal substrate is highly desirable since it allows more precise characterization of its band structure. Electronic band structure characterization is a necessary step for the understanding of the extraordinary magnetic properties of FePt alloy.

For these reasons we here present the study of the *in-situ* growth of a thin film of FePt on a Rh (100) substrate at a temperature lower than 500 ˚C. We select Rh (100), as a seeding substrate for the growth of the FePt alloy, since its lattice parameter (a=3.8Å) is well matched to the in-plane lattice parameter of the L1_0 FePt alloy (a=3.85Å, c=3.71Å). The lattice mismatch between the Rh (100) surface and the FePt L1_0 alloy is of about 1.3%[1]. The Rh (100) surface is also suitable from the

---

[1] Lattice mismatch= $\frac{a_{substrate}-a_{film}}{a_{film}}$ where $a_{substrate}$ and a_{film} are the lattice parameters of the substrate and the film respectively.

chemical point of view since no alloy formation is expected between Pt and Rh at the temperatures considered in this experiment. The study here presented is mainly based on photoemission spectroscopy that is a surface sensitive technique that allow to access to the surface chemical composition and electronic properties of materials.

2. Photoemission spectroscopy

Photoemission spectroscopy (PES) has been established as one of the most important methods to study the electronic structure of molecules, solids and surfaces [5, 6, 10]. Furthermore, PES has widespread practical implications in various fields like surface chemistry or material science, and has significantly contributed to the understanding of fundamental principles in solid state physics.

The story of photoemission spectroscopy began with the discovery of the ***photoelectric effect*** (see Fig. 2.1). In 1887 Heinrich Hertz and Wilhelm Hallwachs demonstrated that negative charges can be removed from a solid when its surface is irradiated by ultraviolet (UV) light.

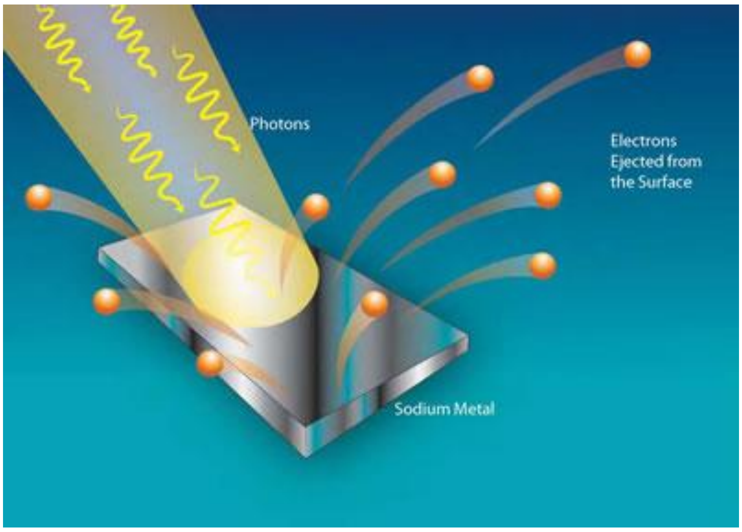

Figure 2.1 The photoelectric effect: electrons are emitted from matter as a consequence of the absorption of energy from electromagnetic radiation [11].

At that time, nobody was able to explain satisfactorily these observations and many experiments followed the observation of Hertz and Hallwachs. Finally, in 1905 Albert Einstein introduced the concept of photon and deduced the relation between the photon energy $h\nu$ and the maximum kinetic energy ${E_{kin}}^{max}$ of the emitted electrons, i.e. the fundamental photoelectric equation

$$\mathrm{E}_{\mathrm{kin}}^{\mathrm{max}} = \mathrm{h}\nu - \Phi_0 \qquad \textbf{(1)}$$

where h is Planck constant, ν the frequency of incident photon and Φ_0 characteristic constant of the sample surface, today known as work function. It was quickly clear that photoelectric effect could be used to study fundamental properties of elementary particles but it was not until 1950's when Kai Siegbahn developed theory and instrumentation for photoemission spectroscopy method known and used today.

2.1 X-ray photoelectron spectroscopy (XPS)

XPS relies on the photoelectric effect. In the simplest picture, the photons which hit the solid kick out electrons which are detected outside. The photon energy must be high enough for the electrons to overcome the work function of the solid. The electron energy distribution outside the solid reflects the density of states inside it (see Fig. 2.2).

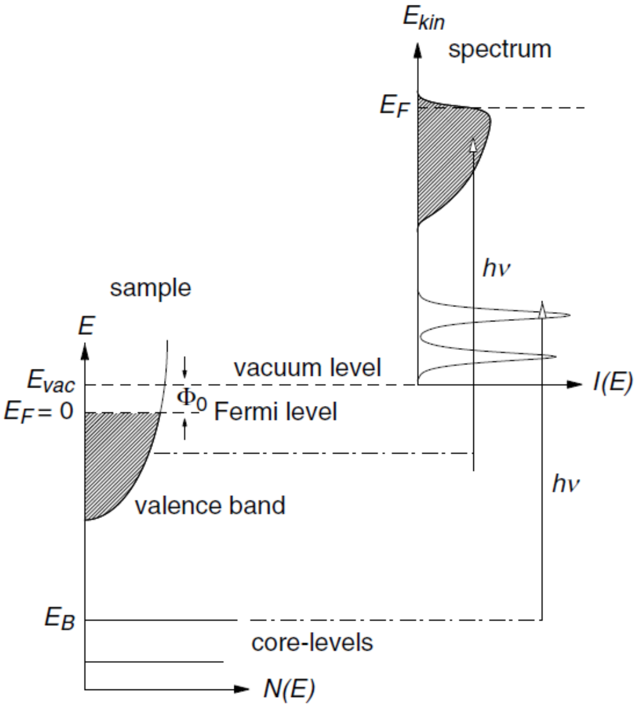

Figure 2.2 Schematic view of the photoemission process [5].

This simplified picture shows the attractiveness of XPS. Electrons with binding energy E_B can be excited above the vacuum level E_{vac} by photons with energy $h\nu > E_B + \phi_0$. The photoelectron distribution $I(E_{kin})$ can be measured by the analyzer and is—to first order—an image of the occupied density of electronic states $N(E_B)$ in the sample. We shall see later that this simple picture is rather poor, in particular for spectroscopy of the valence states.

2.1.1 Qualitative analysis: typical spectra

A typical photoemission spectrum is shown in Fig.2.3. The spectrum was acquired during the Rh (100) sample preparation and measured with a photon energy 630 eV. One can clearly see the spin orbit split Rh 3*p*, 3*d*, 4*p* core levels and the valence band (VB) close to the Fermi level together with some Auger transitions. When using synchrotron radiation, it is simple to distinguish between the Auger and the XPS peaks: One takes the same spectrum at slightly different photon energy. The XPS peaks will shift in kinetic energy by the same amount but the Auger peaks will not, since they leave the sample with a fixed kinetic energy. The possibility of moving the photon energy is also very useful if some adsorbate XPS peaks fall too close to some substrate Auger peaks and are therefore invisible. The background intensity, increasing towards higher binding energies, is due to secondary electrons, i.e. photoelectrons that are inelastically scattered in the sample before escaping into the vacuum.

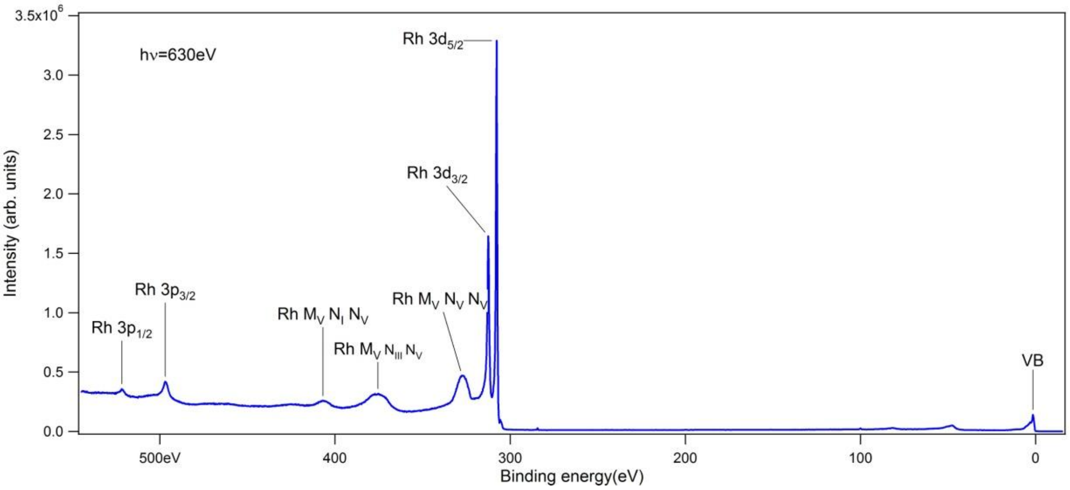

Figure 2.3 Spectrum of clean Rh (100) surface with identified core levels and Auger transitions

Meanwhile, there exist tabulated values for the core-level binding energies and photoemission cross-sections of all elements. The atomic subshell photoemission cross sections have been calculated for isolated atoms by Yeh and Lindau [7]. With this knowledge, it is relatively easy to analyze a photoemission spectrum quantitatively and determine the ***element composition of a sample*** with an accuracy of a few per cent. Furthermore, there is a dependence of the exact binding energy of a core-level on the chemical environment and the valence state of the emitting atom, the so-called ***chemical shift***. These two aspects, together with the high surface sensitivity, make XPS an ideal tool for the chemical investigation of surfaces and thin film.

2.2 Measuring the electronic structure of surfaces with angle-resolved photoemission

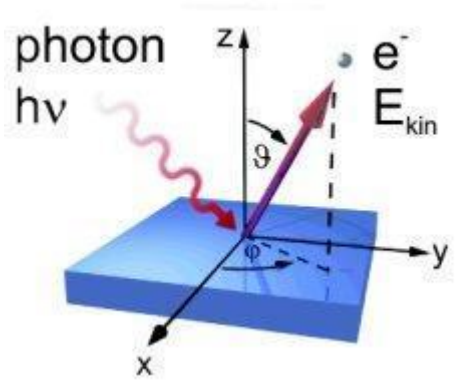

Figure 2.4 In Angle-resolved photoelectron spectroscopy the I (Ekin, hν,θ,φ) could be used to determine the occupied band structure of a crystal.

In angle-resolved photoemission spectroscopy (ARPES) one illuminates a surface with UV light and detects the emitted electrons (Fig.2.4). The spectrometer is designed such that it accepts just a small solid angle and analyses the energy-distribution of the electrons emitted in that solid angle. As we shall see below, angle-resolved photoemission is the technique for the determination of surface (and bulk) band structures. It was developed in the mid-70s [8]. Before, the photoelectron distribution from a sample was only measured in an angle- integrated way, i.e. I (E_{kin}, hν). It was then that people realized that angle-resolved photoelectron spectroscopy I (E_{kin}, hν,θ, φ) could be used to determine the occupied band structure of a crystal. The basic idea is very simple: one determines the energy and all three components of the *k* vector of the emitted electrons. From this one tries to infer E(*k*) inside the solid, i.e. the occupied band structure. A necessary ingredient for the success of ARPES was the development of synchrotron radiation, the ability to change the photon energy continuously is of high importance.

2.2.1 The three step model

In Fig. 2.4 the typical experimental geometry for an ARPES experiment is shown. Monochromatic photons with energy hν are incident on the sample. Electrons are ejected from the sample, as a result of photoelectric effect, and reach the detector, where both the kinetic energy and the emission angle of the electrons are recorded. The photoemission process is usually described by a three-step model developed Berglund and Spicer in 1964 [910]. This is a phenomenological model, but it contains the essential physics of photoemission.

Within this approach, the photoemission process is subdivided into three independent and sequential steps (see Fig. 2.5):

(1) Optical excitation of the electron in the bulk.

(2) Travel of the excited electron to the surface.

(3) Escape of the photoelectron into vacuum.

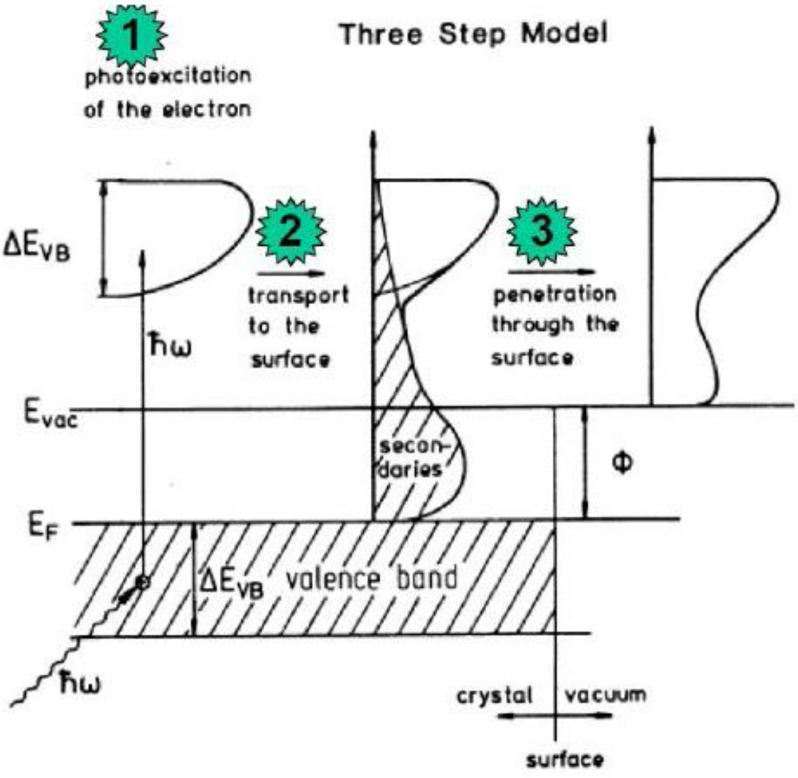

Figure 2.5 Understanding the photoemission process based on the three-step model [9].

In step (1), an occupied electronic state (initial state) is excited into an unoccupied state (final state) through photon absorption. Because the photons impart very little momentum, the momentum of the electron is essentially unchanged. Step (2) can be described in terms of an effective mean free path which is proportional to the probability that the excited electron will reach the surface without scattering. The inelastic scatterings of electrons give rise to a continuous background in the photoemission spectra which is usually ignored or subtracted. Once the electron reaches the surface (step (3)), it overcomes the work function of the material and eventually emits from the surface. Within this process, the momentum perpendicular to the surface is not conserved, and the electron is refracted in a similar manner to that of light at the interface between two materials (see Fig.2.6). Nevertheless, the parallel component of the momentum is still conserved (analogous to Snell's Law).

The energy conservation requires:

$$E_{kin} = h\nu - |E_B| - \Phi \tag{2}$$

$$k_{||\,i} = k_{||f} = \sin(\Theta)\sqrt{\frac{2\,m}{\hbar^2}}\sqrt{E_{kin}} = \sin(\Theta)\sqrt{\frac{2\,m}{\hbar^2}}\sqrt{h\nu - E_B - e\Phi}$$

Where $k_{||i}$ and $k_{||f}$ are the parallel wave vector of the initial and final states, θ is the polar emission angle (Fig. 2.6). E_{kin}, Φ and θ can all be measured directly from the experiment. Therefore, the energy and in-plane wave vector of the electronic state before photoemission can be determined from Eqs. (2) and (3). The results from an ARPES measurement are generally expressed as a three-variable photocurrent function I (E_B, k_x, k_y). Tracing the peaks in the photocurrent function allows us to obtain the in-plane dispersion of the occupied band. A plot of photocurrent as a function of energy for a fixed (k_x, k_y) is called the energy distribution curve, while the momentum distribution curve refers to the photocurrent as a function of $k_{||}$ at a fixed energy E_B. Moreover is possible to collect photoemission data in a bi-dimensional (2D) matrix (***photoemission intensity map***, see Sec. 3.4*)*, with one axis being the electron's kinetic energy and the other one being the emission angle along a certain direction (see Sec). The perpendicular momentum of the initial state, $k_\perp$, cannot be determined from ARPES in a direct manner. Extracting $k_\perp$ requires knowledge of the final state dispersion, which is generally complicated. This k□ problem is not an issue for two dimensional (2D) systems, because there is no dispersion along the *z* direction. The system studied in this thesis is in this category.

The three-step model is only a phenomenological model, because the division of the photoemission process into three steps is artificial and unrealistic. A more accurate theory of photoemission involves the rigorous quantum-mechanical treatment.

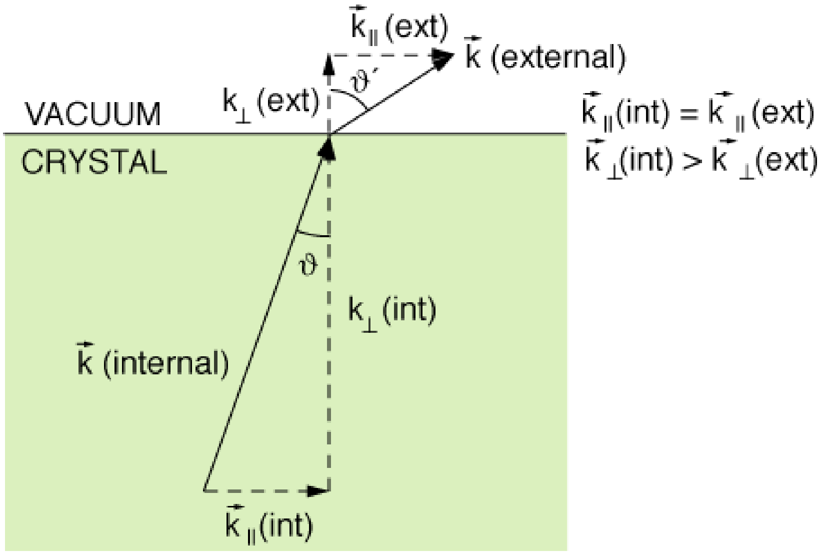

Figure 2.6 Refraction at the surface potential barrier [11].

3. Experimental set up for photoemission experiments with synchrotron radiation

Photoemission spectroscopy is notable for its surface sensitivity. It allows probing surface-related electronic states and the surface chemical composition. Photons have no trouble penetrating crystal samples, but the short mean-free path of photoelectrons limits the probe depth (step (2) in the three-step model, see Sec.2.2.1). Fig. 3.1 displays a plot of the experimental mean free path λ of electrons as a function of the kinetic energy. This shows that λ is almost material independent. Due to the constraint from the photoemission cross section, as well as the momentum resolution, photoemission experiments are typically carried out with the kinetic energy of electrons in the range of 10-1000 eV. This indicates that the useful photoemission intensity comes from the first few atomic layers of the material. The surface sensitivity of photoemission requires that the sample surface stays clean and free of contamination during the measurement [6, 11].

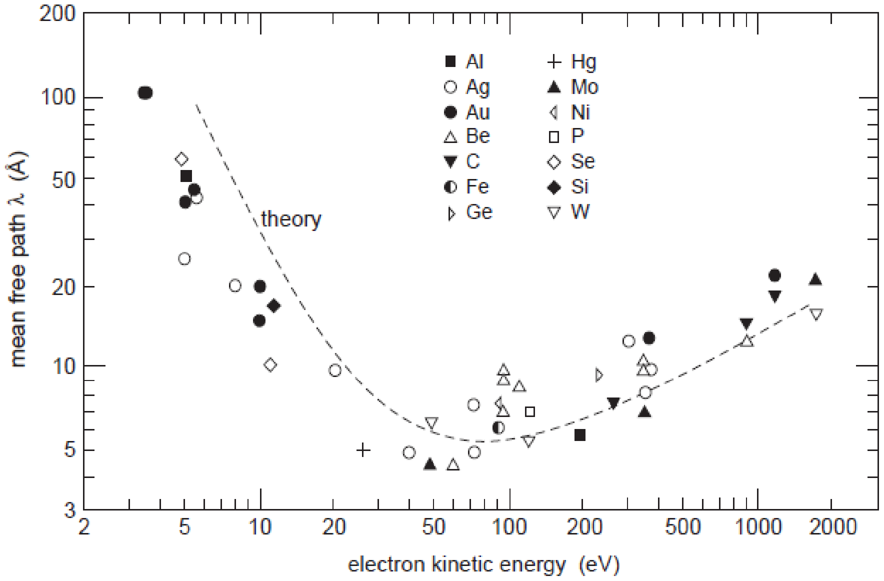

Figure 3.1 Mean free path of electron in solid (λ) as a function of electron kinetic energy. The dots are measurements; the dashed line is a calculation

3.1 Ultra high vacuum

In order to keep the sample free of contamination during the measurement, the chamber must be under ultrahigh vacuum (UHV).

UHV is term used for describing pressures lower than 10 nanopascals (10^{-8} mbar). Achieving such conditions is not trivial and requires special procedures, equipment and tools [10, 12].

One can notice benefits of such a system considering the average molecular flux per unit surface area in unit time at pressure P and temperature T that is given by the formula:

$$F = \frac{p}{\sqrt{2\,\pi\,m\,k\,T}} \tag{4}$$

where m and k are the molecular mass and Boltzmann constant, respectively. At the pressure of about 10^{-6} mbar and room temperature, the surface will become completely covered by gas molecules in approximately 1 second, assuming that every gas molecule that hits the sample surface will stick. Therefore, keeping the sample free of contamination for several hours means that a pressure typically in the range of 10^{-10} mbar is preferred.

A routine procedure for reaching UHV in our chamber is as follows: First, the chamber must be leak-tight, particularly at the joints of flanges. Rotary and turbo pumps are used initially to provide the minimum vacuum (typically < 10^{-5} mbar) required to start the ion pump. Once the ion pump takes over, the chamber can achieve a pressure of ~10^{-8} mbar within a few hours. In order to obtain the pressure required for photoemission measurement, a “bakeout” of the chamber is carried out, during which the chamber is heated to 150ºC for about 24 hours. In this process, most of the gas molecules that are absorbed by the inner walls of the chamber are pumped out by the ion pump. After the bake out, the titanium sublimation pump is used periodically to provide additional pumping power in the chamber. Attaining and preserving UHV condition in the chamber is a prerequisite for a successful photoemission experiment. Common sources of bad vacuum include leaks at the joints of flanges, UHV incompatible materials inside the chamber, etc. UHV incompatible materials, which generally have a large vapor pressure and cannot be removed by the bake-out procedure, include, but are not limited to, a majority of organic compounds, normal glues, and lead solder. One should ensure that the material is UHV compatible before putting it into the vacuum chamber.

3.2 The light source

All of the photoemission experiments in this thesis were carried out at VUV beamline at Elettra synchrotron radiation facility. In comparison with other laboratory light sources that use the characteristic emission lines of specific elements, the synchrotron light source is superior in terms of its high intensity, high level of polarization, high collimation, wide tune-ability of photon energy (from infrared to hard X ray)

3.2.1 Synchrotron light source

Synchrotron is a type of particle accelerator used primarily as a light source. Synchrotron light is produced by electrons forced to follow a circular orbit [13]. A schematic view of a synchrotron is shown in Fig. 3.2

Electrons are emitted from ceramic disc heated to the very high temperature in the electron gun and accelerated with electric field to 100keV in linear accelerator called LINAC Series of quadruple magnets are placed between boosters to guide the beam. A low energy bunching system gathers electrons into groups and two high energy 5m long radio-frequency structures operating at 3 GHz accelerate them to 100 MeV. Particles are then guided into the booster, which is basically a small synchrotron with a circumference of 112 m and accelerated in cycles to a final energy of 2-2.4 GeV. The last step is the ejection of those electrons into the storage ring.

The storage ring is not circular, despite its name, but a polygon. A dipole magnet generating a magnetic field of 1.5T is placed in every corner to bend the electron beam trajectory. Focusing is achieved with series of quadruple magnets.

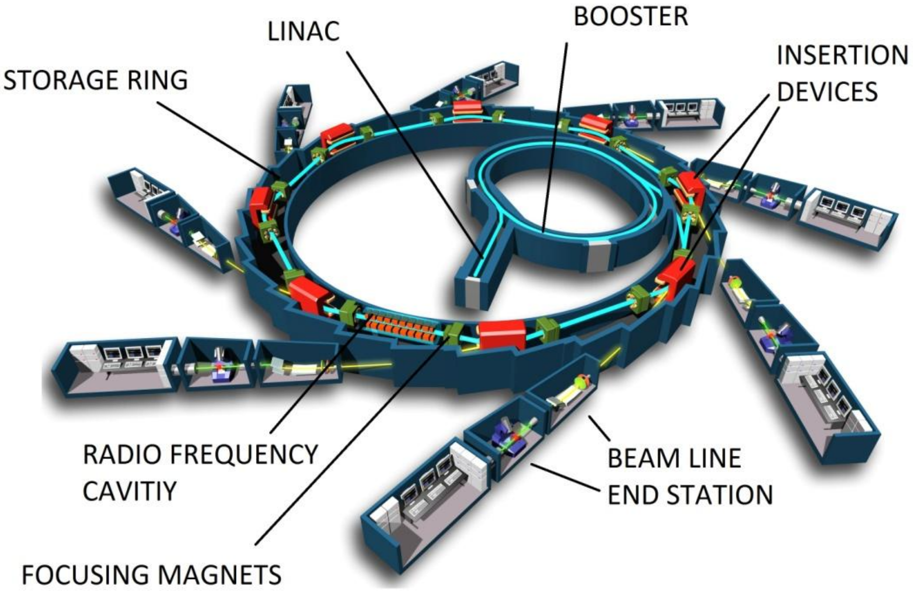

Figure 3.2 Schematic view of a synchrotron facility [14]

Electrons loose energy in the bending magnets that it is recovered by placing radio-frequency cavities in the storage ring.

The very last part of synchrotron installation is dedicated to the production and distribution of light to the beamlines. Synchrotrons of the first generations used light from bending magnets but latest versions use specially designed insertion devices: wigglers and undulators. The working principle of wigglers and undulators is the same as in the bending magnets. The main difference is the coherency of magnetic field to which the electrons are subject. They consist of series of reversely oriented magnets, which forces the electrons to follow a wavy trajectory. This produces synchrotron light with high brilliance.

At Elettra synchrotron there are currently 26 beam lines, including a storage-ring free-electron laser. All of the most important x-ray based techniques in the areas of spectroscopy, spectro-microscopy, diffraction, scattering and lithography are present, together with facilities for infrared microscopy and spectroscopy, ultraviolet inelastic scattering, and band mapping. Versatile experimental stations are maintained at the state-of-the art, offering unique means to carry out outstanding research in diverse fields and disciplines.

3.2.2 The VUV photoemission beamline

The VUV photoemission beamline has been designed primarily for characterization of surfaces and solid state materials by means of high resolution photoemission experiments. The light source is an undulator with a range of **17** to **900 eV**. The undulator of the VUV beamline consists of 36 periods, divided in three sections. The photon flux on the sample is energy dependent and varies from 1.4 x 10^{13} to 5 x 10^{10} photons/sec/0.1%bw/200mA, in a spot of maximum size 0.5 mm. The beamline is controlled via the beamline control system (BCS) software.

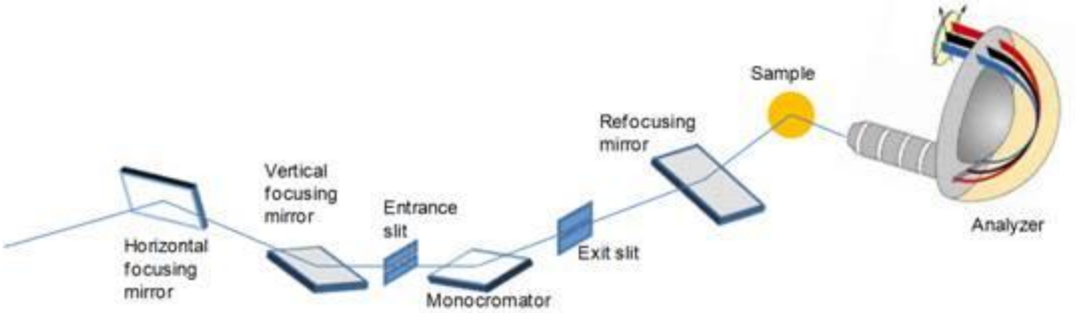

Figure 3.3 VUV beamline schematic illustration [13]

The Kirkpatrick-Baez entrance optics focuses the light after the entrance slit of the monochromator. The monochromator is a Spherical Grating Monochromator with five interchangeable gratings and pre and post-focusing optics. The set of five gratings provides a resolving power of 10,000 over the whole energetic range. The light emerges from the movable exit slit and is then refocused by a post-focusing mirror onto the sample. For lower photon energies (< ca.130 eV), the angle of deflection of the light at the grating is increased from 7° to 20° and requires an additional pair of plane mirrors to refocus, one of which is fixed and the other removable.

3.3 The end station for photoemission experiments

The end station of VUV beamline is composed by a two interconnected UHV chamber separated by a valve: preparation chamber and measurement chamber.

3.3.1 The preparation chamber

The preparation chamber (see Fig. 3.4, 3.5) is UHV set-up devoted to the *in-situ* preparation of surfaces and nanostructured materials such as thin films, monolayers, wires etc. that are characterized by means of photoemission in the measurement chamber. The base pressure is 10^{-10} mbar. Samples are mounted on a horizontal manipulator that allows six degrees of freedom (x, y, z, θ and tilt angles) with high precision. A fast entry load lock allows transferring the samples from ambient pressure to UHV without affecting the vacuum conditions. The manipulator length allows the transfer of the sample between preparation and measurement chamber. The instruments available for the preparation of surfaces and nanostructures are: ion gun for Ar^+ sputtering, LEED apparatus, various changeable evaporators and microbalance for evaporation calibration. Gas inlet into the preparation chamber is done using a dedicated “gas dosing facility”. We inlet O_2 during the Rh (100) surface preparation. Onto the manipulator the sample holder allow to heat up the sample by direct current flow (low temperature regime ~800˚C). To reach higher temperature the sample need to be transfer in an independent heating chamber attached to preparation chamber (~2200˚C). In this experiment we annealed the Rh(100) surface onto the independent heating chamber (flash at ~1000˚C). The sample can be cooled down up to 100 K using a liquid nitrogen cryostat installed into the manipulator.

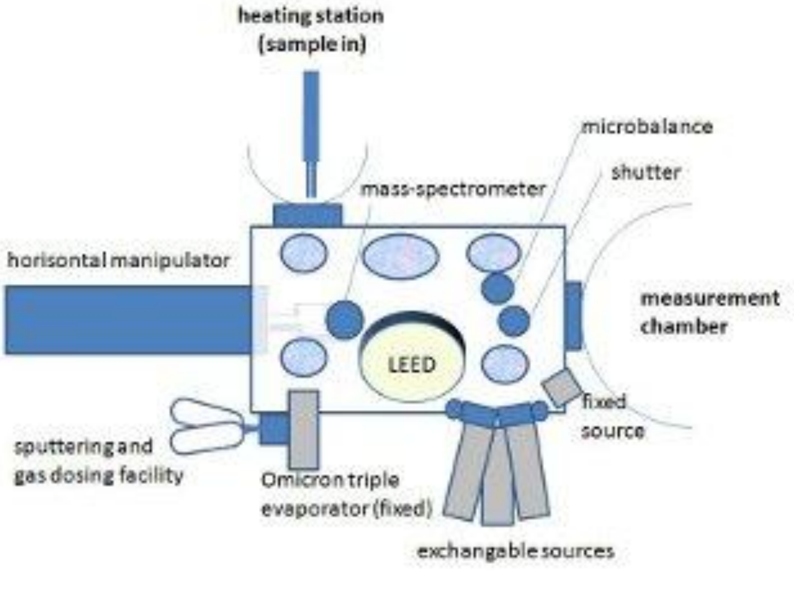

Figure 3.4 Schematic view of the preparation chamber at VUV beamline [13]

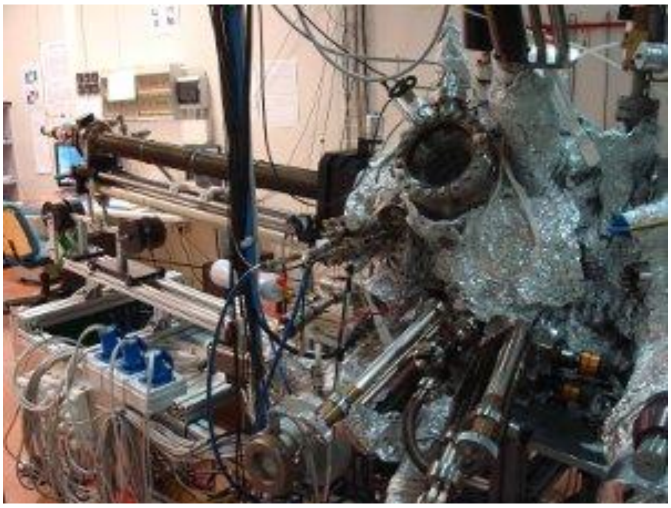

Figure 3.5 Photo of preparation chamber at VUV beamline [13]

3.3.2 The measurement chamber

Photoemission measurements are done in the measurement chamber (Fig.) at pressure of 10^{-11}mbar. The chamber is equipped with a vertical manipulator that allows Fermi surface measurements by computer controlled azimuthal rotations. The electron analyzer is a SCIENTA R4000 spectrometer with more than 30° acceptance angle, mounted 45° to the beam direction.

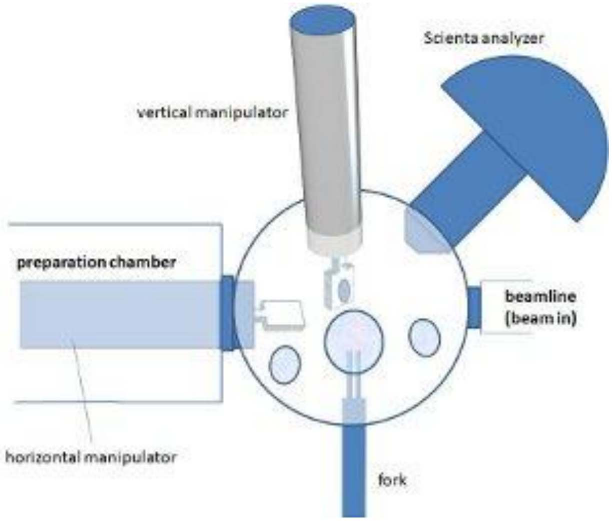

Figure 3.6 Schematic view of experimental chamber at VUV beamline [13]

Figure 3.7 Photo of experimental chamber at VUV beamline [13]

3.4 The concentric hemispherical electron analyzer

At VUV beamline photoemission experiment are performed using a concentric hemispherical analyzer (CHA) Scienta R4000. The logical components of the analyzer are shown in Fig. 3.8[6, 10]. Photons illuminate an area of the sample causing electrons to be ejected with a range of energies and directions. The electron optics, which is a set of electrostatic lens units with a cylindrical shape, collects a proportion of these electrons that are transferred through the apertures and focused onto the analyzer *entrance slit*.

An electrostatic field applied between two precisely machined concentric hemispheric electrodes with radius R1 (inner) and R2 (outer) allows electrons of a given energy (the so called *Pass Energy* PE) to arrive at the detector slits.

Negative potentials V_1 and V_2 are applied to each hemispherical plate where $V_2>V_1$. The potential V_0 across the median hemispherical surface between the two plates is:

$$V_o = \frac{V_1 R_1 + V_2 R_2}{2R_0} \tag{5}$$

When emitted photoelectrons with energy $E=eV_o$ tangentially enter median surface at radius R_0 their circular orbits will follow equation.

$$e\,\Delta V = E\left(\frac{R_2}{R_1} - \frac{R_1}{R_2}\right) \tag{6}$$

Where ΔV = V_2-V_1. If an electron has exactly the energy V_o its trajectory will follow this radius. Electrons that enter the hemispheres with a kinetic energy different from V_0 are not allowed to circulate and therefore do not reach the exit slits.

Electrons of a specific initial kinetic energy are measured by setting voltages for the lens system that focus onto the entrance slit the electrons of the required initial energy and retards their velocity so that their kinetic energy after passing through the transfer lenses matches the pass energy of the hemispherical analyzer. To record a spectrum over a range of initial excitation energies it is necessary to scan the voltages applied to these transfer lenses and the prescription for these lens voltages is known as the set of lens functions. These lens functions are typically stored in the configuration file used by the acquisition system.

The efficiency with which electrons are sampled by a spectrometer depends strongly on these lens functions. Different transmission function has been obtained during the commissioning of the instrument for the different lens mode and energy resolution.

A hemispherical analyzer and transfer lenses can be operated in two modes, namely, Fixed Analyzer Transmission (FAT), also known as Constant Analyzer Energy (CAE), or Fix Retard Ratio (FRR) also known as Constant Retard Ratio (CRR).

In the experiments here presented we used FAT mode. In FAT mode, the pass energy of the analyzer is held at a constant value and it is entirely the job of the transfer lens system to retard the given kinetic energy channel to the range accepted by the analyzer.

In FAT mode the energy resolution remains independent of the kinetic energy of the electrons. E_0 is held at some constant value, typically in the range 5-20 eV. This is commonly referred to as the pass energy, with lower values resulting in improved resolution, but increased acquisition times.

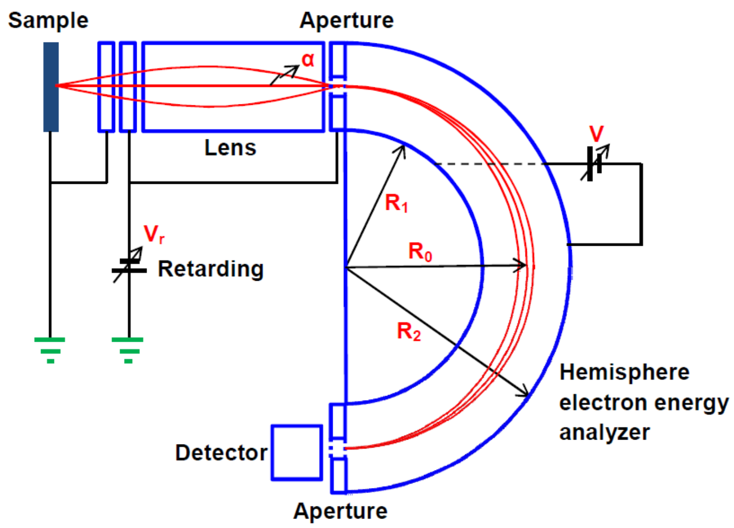

Figure 3.8 Schematic of a hemispherical electron analyzer

The most important parameter of an electron analyzer is the energy resolution, which is determined as the ratio

$$\frac{\Delta E}{E_o} = \frac{s}{R_0} \tag{7}$$

where s is the mean pass slid width.

In FAT mode the energy resolution remains independent of the kinetic energy of the electrons since E_0 is held at the pass energy value. In the set-up used for the experiments reported in chapter 4 the pass energy is 10 or 20 eV. With these values the energy resolution of the analyzer is 2 to 5 meV.

When electrons reach the exit slit they are collected by a two-dimensional detector (2D) system (see Fig. 3.8). The position where an electron hits the 2D detector is determined by the electron’s kinetic energy and emission angle. The exact conversion between the positions on the detector and the electron’s kinetic energy/emission angle is taken into account in the Scienta software. The resulting data after one scan is a 2D matrix (***photoemission intensity map***), with one axis being the electrons kinetic energy and the other one being the emission angle along a certain direction (see Fig. 3.9). The angular range is 30° degrees in our analyzer. Photoemission intensity maps are obtained by using the formula (3), which establish the relation between emission angle θ, kinetic energy E_{kin} and $k_{||}$:

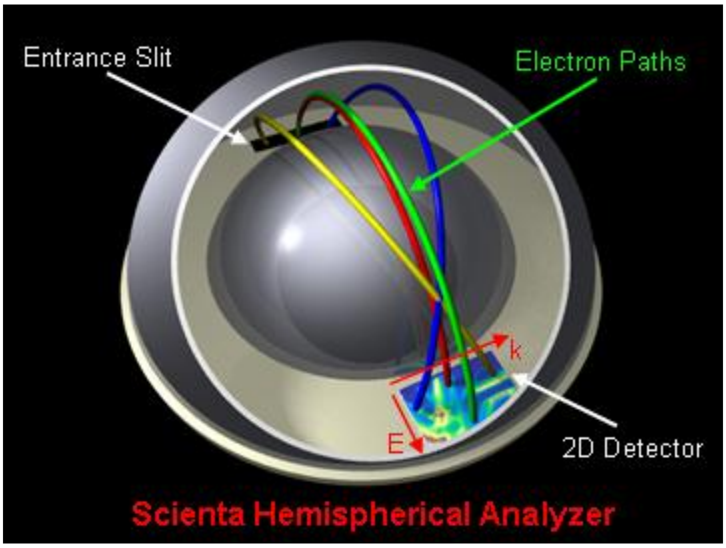

Figure 3.9 Schematic of Scienta electron analyzer with 2D detector -energy and emission angle ($k_{||}$ momentum) [15]

3.5 LEED

LEED stands for low energy electron diffraction and it is one of the most commonly used methods for investigation of surfaces [10]. It can be used qualitatively to determine surface structure and periodicity or quantitatively to determine atomic distances with comparison to the calculated values.

LEED basis is diffraction of sent electrons on electron density on surface atoms. Electrons are produced by an electron gun and led perpendicular to the surface with well-defined energy from 20-200eV. This range of energy corresponds to distance between surface atoms or molecules 2.7-0.87 Å since the wavelength of the electrons is given by the de Broglie relation $\lambda=h/p$ where p is the electron momentum and h is the Planck constant. The relation between the wave length and the electron energy E is given by:

$$p = m\,v = \sqrt{2\,m\,E} = \sqrt{2\,m\,e\,V}\,, \lambda = \frac{h}{p} = \frac{h}{\sqrt{2\,m\,e\,V}} \qquad (8), (9)$$

where m is the electron mass, v the electron velocity.

The apparatus, shown in Fig. 3.10, is made from four grids, first is kept on ground potential to ensure field free region around the sample, next two grids are kept on potential little bit smaller than electron energy to reflect all non-elastically scattered electrons and last one again being on ground potential. Image is generated on fluorescence screen set to high voltage. Behind the screen there is a window that allows observation of the images.

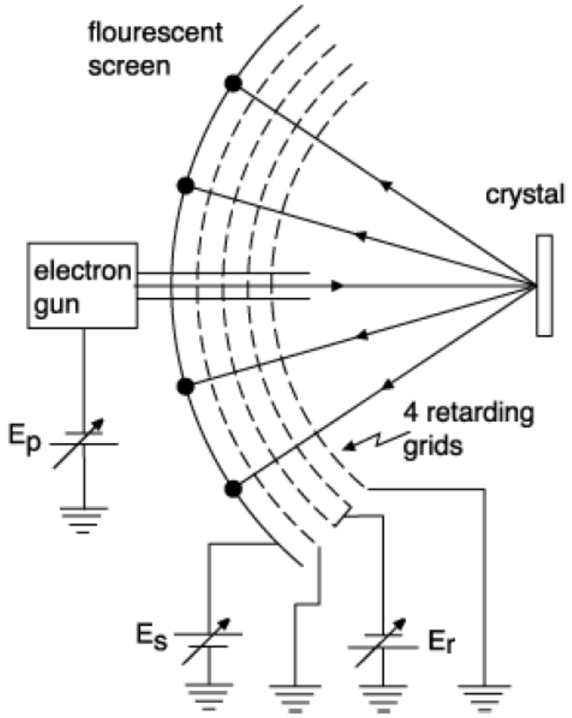

Figure 3.10 Schematic view of LEED apparatus [11]

Diffraction conditions for the two dimensional systems are similar to those of three dimensions and are given by the Laue conditions:

$$\left(\overrightarrow{k_i} - \overrightarrow{k_f}\right) \overrightarrow{a_1} = 2\,\pi\,h, \quad \left(\overrightarrow{k_i} - \overrightarrow{k_f}\right) \overrightarrow{a_2} = 2\,\pi\,k \qquad (10), (11)$$

Where k_i and k_f represent the primary (incident) and secondary (emerging) wave vectors, a_1 and a_2 are the are the two-dimensional lattice vectors, h and k are arbitrary integers. We know that this condition is fulfilled by any vector in reciprocal lattice which gives us the diffraction condition associated with the momentum transfer parallel to the surface ($\Delta k_{||}$):

$$\Delta\overrightarrow{k_{||}} = h\,\overrightarrow{g_1} + k\,\overrightarrow{g_2} \qquad (11.a)$$

where g_1 and g_2 are the reciprocal lattice vectors of the surface.

Energy conservation imposes the restriction:

$$|k_i| = |k_f| \qquad (11.b)$$

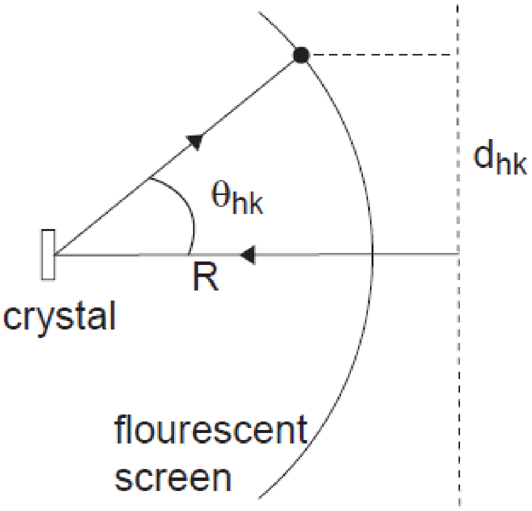

Figure 3.11 Imaging of the reciprocal lattice by LEED [11]

In most cases the electron beam hits the surface at normal incidence, i.e. such that $k_{||}$ is 0 for the incident electrons. In this case the resulting diffraction patterns maxima can be directly associated with the reciprocal lattice and it represents the symmetry of the surface. In fact, for such a system the diffraction pattern will be an image of the surface reciprocal lattice.

According to equation (11.a) we will find high intensity at:

$$\Delta\overrightarrow{k_{||}} = \overrightarrow{k_{||}} = h\,\overrightarrow{g_1} + k\,\overrightarrow{g_2}$$

The magnitude of the outgoing electrons is given by (12.b) and this give the magnitude of the emission angle $\sin\theta_{hk}=|k_{||}|/||k|$.

If we consider the LEED apparatus (see Fig. 3.11) the intensity maxima on the screen is given by:

$$d_{hk} = R\sin\Theta_{hk} = \frac{R}{|k|}\left|(h\overrightarrow{g_1} + h\overrightarrow{g_2})\right| = R\sqrt{\frac{\hbar^2}{2m}\frac{1}{\sqrt{E}}}\left|(h\overrightarrow{g_1} + h\overrightarrow{g_2})\right| \qquad (12)$$

During our experiments we performed qualitative LEED measurements in order to have immediate and direct information about the surface order and quality. We used also to establish the correct sample prior valence band dispersion measurements.

When the surface is reconstructed or covered with adsorbents, the LEED images can quickly give some information about the surface symmetry and periodicities.

3.6 Fe and Pt evaporators

Electron beam evaporators were used for Fe and Pt deposition [10]. In Fig. there is a schematic view of the evaporators used during the experiment. Electron emitted from a W filament heated by passing current. The electrons emitted by the W filament are accelerated by high positive voltage (about 1KV) onto the tip of the material rod that we want to evaporate (Fe and Pt). High purity (99.99% purity) Fe and Pt rods (1mm diameter) are used. The vapors travel through vacuum and deposit uniformly on sample surface. Before starting any deposition on to a clean sample, the rods have to be clean *in-situ* by standard outgassing procedure.

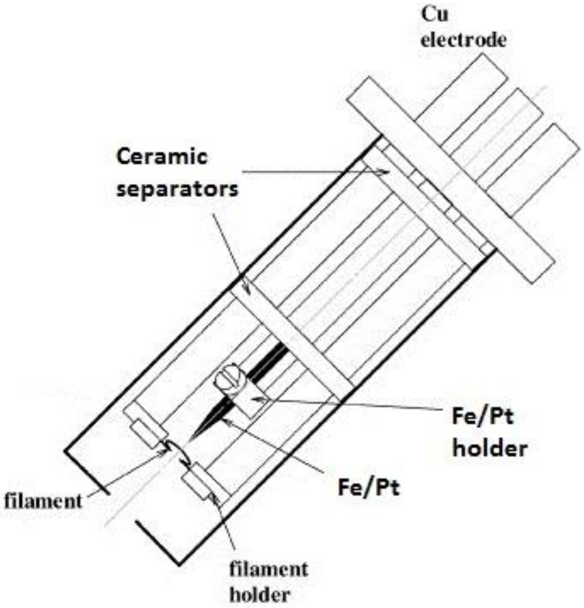

Figure 3.12 Schematic view of the Pt and Fe electron beam evaporators.

4. Characterization of growth and electronic properties of a FePt alloy film on the Rh (100) surface[2].

4.1 In situ Rh (100) surface preparation

Surface science experiments are usually dedicated to the investigation of surface properties, which, by definition, depend on the status of the topmost layers of the samples. This implies that single-crystal samples used in our study had to be properly treated to achieve atomic level control of the chemical composition and morphology before performing FePt film growth and ARPES experiments.

The sample is transferred from air into the preparation chamber by using the fast entry load lock (see. Sec. 3.3.1). The cleaning procedure of the Rh(100) surface implies the use of a Ar^+ sputtering treatment. This is achieved by ionizing and accelerating argon atoms that are introduced into the preparation chamber to bombard the sample surface. This process removes the contamination on the surface and exposes clean regions of the crystal. The sputtering is normally followed by a sequential annealing, which restores the order of surface structure previously destroyed by the argon bombardment. The argon pressure for sputtering is of about 3×10^{-6} mbar. The accelerating voltage and emission current of the sputter gun filament is typically 1-1.5 kV and 25 mA, respectively. The duration of the sputtering was decided step by step to optimize the preparation procedure. The annealings were done at about 1000˚C with duration of the order of few minutes. The temperature onto the sample was measured with an infrared optical pyrometer.

---

[2] All the data presented in this work was analyzed and plotted using Igor Pro 6.12 software.

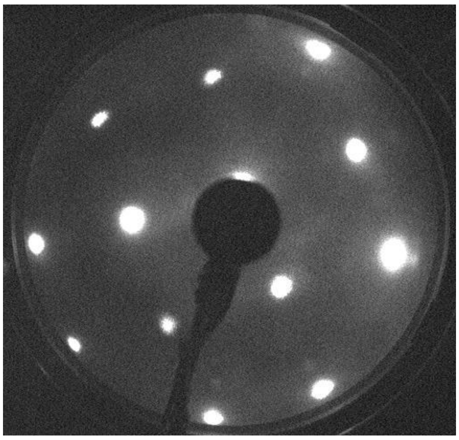

Figure 4.1 LEED patter of Rh (100). Incident beam energy E_P=100eV

The crystalline quality and chemical composition of the sample were checked by LEED and XPS measurements after few cycles of sputtering and annealing. The LEED pattern of Rh (100) surface is the depicted in Fig. 4.1.

The LEED characterization gives information about surface order. When a good LEED pattern was obtained, XPS measurements were performed in order to determine the chemical composition of sample surface. This is necessary because various impurities reside within material as natural contaminants or residuals of the single crystal fabrication. Contamination of the top layers can also occur during the fine mechanical polishing of the surface done *ex-situ*. Once the contaminants are identified different strategies are used to remove them.

In Fig.4.2 we report wide energy photoemission spectra collected at different stages of the Rh (100) cleaning procedure.

The first spectrum (blue line) was acquired after the first cycle of sputtering at 1KV for 80 minutes. Apart from Rh core levels (Rh 3*p*, Rh 4*s*, Rh 4*p*) and the Rh(100) valence band, we identify C and Ar peaks (C 1*s* and Ar 2*p*).

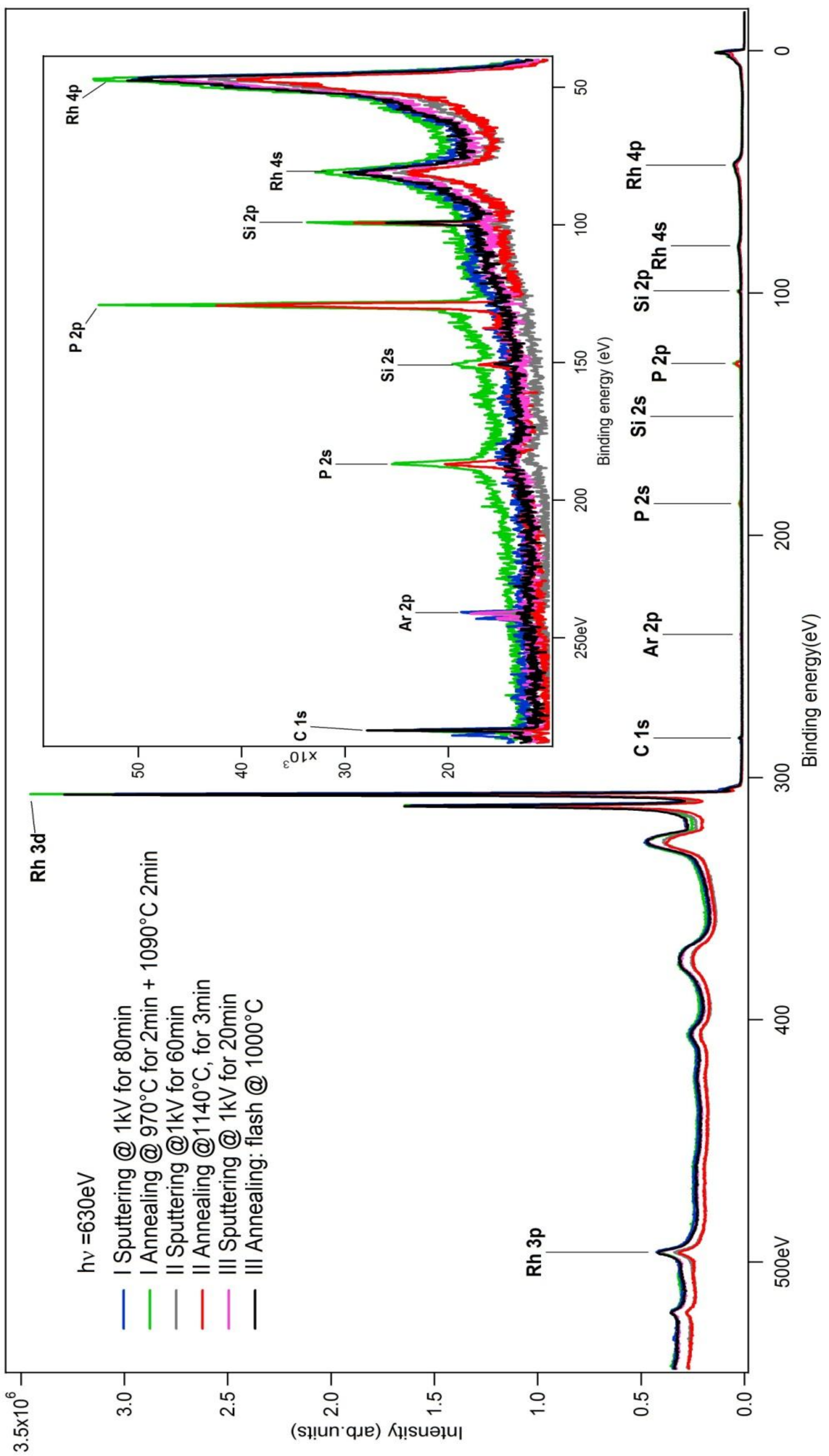

Figure 4.2 XPS wide energy spectra measured at the different stage of the Rh(100) surface preparation. The spectra are measured with photon energy of 630 eV. Different chemical species are identified by labeling the corresponding core level features present in the spectra.

Usually, for rhodium samples, carbon is the main contaminant and to remove it annealing the sample (about 1000 °C) in oxygen rich atmosphere (10^{-7}mbar) is routinely done. At this high temperature the carbon contaminants present on the surface react with O_2 forming CO which is then pumped out of the system. Ar is observed due to the adsorption of some Ar atoms during the sputtering procedure. These atoms are easily removed by a gentle annealing. After a first annealing in O_2 atmosphere for 2 minutes at 970 °C and 2 minutes at 1090 °C the XPS spectrum we obtained is the green spectrum in Fig.4.2. We observed a decrease of C, but the appearance of other peaks due to new chemical species present onto the Rh surface. We identified them through their characteristic binding energies as P (P 2*s* and 2*p* core levels) and Si (2*s* and 2*p* core levels).

The subsequent Ar^+ sputtering of 1 hour at 1 KV completely removed the P and Si contaminants (grey curve) indicating that they were localized just on the surface. Si was most probably due to contamination occurred during the *ex-situ* mechanical polishing done on the sample using a paste composed by Si, while P is most probably a natural contaminant present in Rh bulk.

After a new annealing was done at 1140 °C for 3 minutes (red curve in Fig.4.2) again P and Si appeared as contaminants. Their contribution diminished with respect to the previous annealing (see green curve in Fig.4.2) indicating that the Si and P contamination diffusion form sub-surface layers is promoted by annealing and increases with the annealing duration. We performed a final sputtering of 20 minutes at 1 KV and very short annealing (flash) at 1000C (always in presence of O_2) and obtained an XPS spectrum without P and a reduced presence of C and Si. Subsequent very short annealing in O_2 at about 1000C further reduced the C and Si contamination.

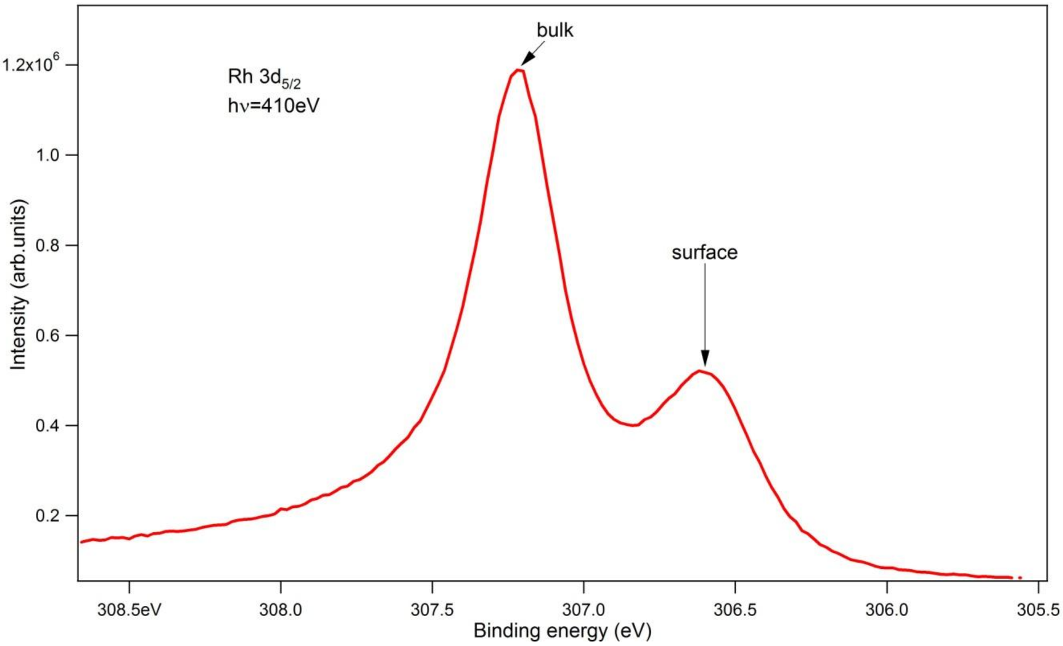

Figure 4.3 XPS spectrum of Rh 3d5/2core levels of Rh (100) clean surface measured with photon energy of 410eV. The energy difference between surface and bulk components is 0.62 eV.

The quality of the preparation was checked by measuring again the LEED pattern and the XPS spectra of the Rh $3d_{5/2}$ core level. The LEED was a good 1x1 pattern with sharper peaks than the one measured after the first stages of sample preparation. The Rh $3d_{5/2}$ core level spectra are shown in Fig.4.3. In the spectrum two main peaks due to the Rh bulk and surface atoms are clearly visible. The energy difference between the two structures is 0.62 eV, in good agreement with the value reported in the literature [16]. This core level shift is related to differences in the coordination of the atoms between the first and deeper layers of the Rh (100) crystal. A well resolved and intense surface component is a signature of high preparation quality of the Rh (100) sample surface[16].

4.2 Fe and Pt evaporation calibration

Before the FePt film growth, Fe and Pt evaporation calibration was done. It is possible to estimate the Pt and Fe coverage by using a simple attenuation model that takes into account the behavior of the XPS Pt (or Fe) and Rh core level spectra with coverage.

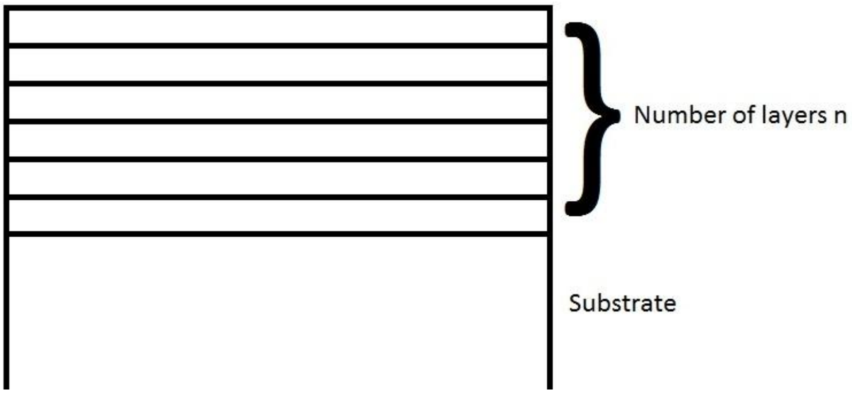

Figure 4.4 Scheme of layer by layer growth. In our case the substrate is Rh (100) and the layers are Pt or Fe.

In the hypothesis that the growth of Pt on Rh (100) is two dimensional (layer by layer, see fig. 4.4) the ratio between the area of Pt *4f* core level (A_{Pt}) with respect to the area of Rh *3d* core level (A_{Rh}) is given by:

$$\frac{A_{Pt}}{A_{Rh}} = \frac{\sigma_{Pt}}{\sigma_{Rh}} \frac{\sum_{i=0}^{n} e^{-i\frac{d_{Pt}}{\lambda_{Pt}}}}{\sum_{i=0}^{\infty} e^{-(i+n)\frac{d_{Rh}}{\lambda_{Rh}}}} \tag{14}$$

where d_{Pt} and d_{Rh} are the spacing between of the Pt and Rh layers, λ_{Pt} and $\lambda_{Rh}$are the photoelectron escape depth of Pt and Rh and n is the number of Pt layers. σ_{Pt} and σ_{Rh} are photoelectron cross sections at given energies, obtained from Ref. [7]

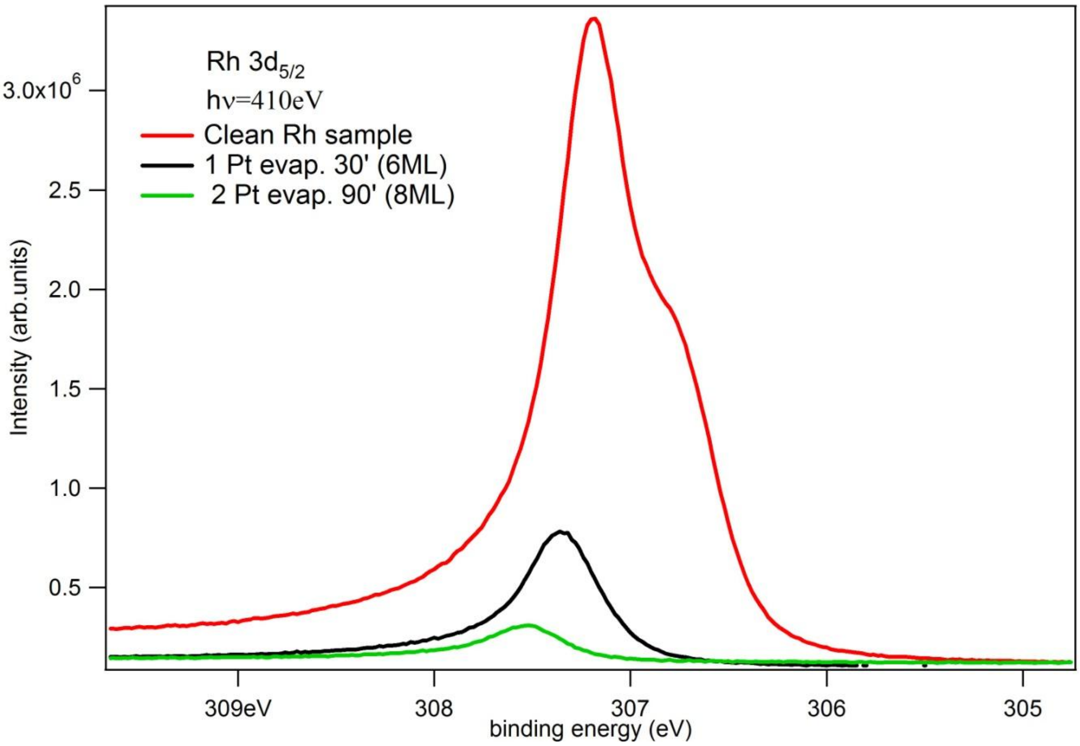

Figure 4.5 Rh 3d5/2 core level spectra of the Rh (100) clean sample and after 30’ and 60’ of Pt evaporation. The spectra were measured with photon energy of 410eV.

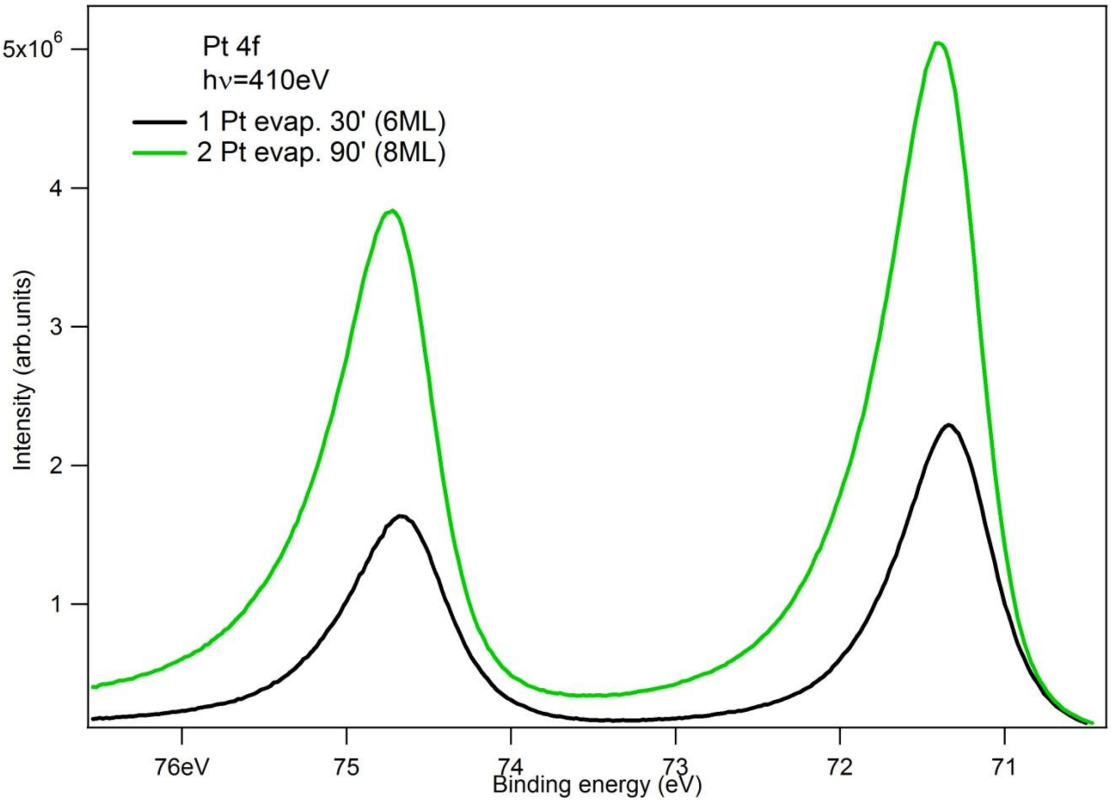

Figure 4.6 Pt 4f core level spectra collected after 30’ and 90’ of Pt evaporation. The spectra are measured with photon energy 410eV.

In Fig. 4.5 and 4.6 we show the Pt 4f and Rh 3$d_{5/2}$ core levels as a function of the Pt evaporation time. The Pt evaporator was an electron beam evaporator as described in Sec.3.6. The Pt evaporations were done setting the filament current at 2 A and the applied voltage of the Pt rod at +1KV with an emission current on the Pt rod of 21 mA.

In the Table 4.1 we report the calculated areas of Rh 3$d_{5/2}$ and of Pt 4$f_{7/2}$ spectra after a linear background were subtracted. The calculated areas were normalized to the corresponding photoionization cross section [7]. We calculated the corresponding coverage in monolayers (MLs) using the Formula (14). In the Formula we assume λ_{Pt} and λ_{Rh} at 300eV electron kinetic energy to be 10 Å, in analogy with the value measured for Ag (see Fig. 3.1). d_{pt} is 3.92Å and d_{rh} is 3.8Å. The Pt evaporation rate obtained for the different evaporations is not exactly the same, probably because of some instability in the evaporator. Since our experiment is focused on the evaporation of few monolayers of Pt at a time we set the evaporation parameters to 0.2ML/min ± 0.05ML/min. The error mainly derives from λ_{Pt} andλ_{Rh}, whose esteem is based on the collection of experimental data reported in Fig. 3.1.

Table 4.1 Calculated areas of Rh 3d3/2 and Pt 4f7/2 core level spectra as a function of Pt evaporation time. Areas normalized to the photoionization cross section and corresponding thickness are also reported.

Pt Evap. Time (minutes)	A_{Rh}	A_{Rh}/σ_{Rh}	A_{Pt}	A_{Pt}/σ_{Pt}	Calculated thickness (ML)	Evaporation rate (ML/min)
0	2.601e+06	645181	0	0	0	0
30	420277	104235	1.73309e+06	385345	6	0.2
90	115259	28586.1	4.04695e+06	899822	8	0.09

After the last Pt evaporation, we performed a set of measurements to check the thickness homogeneity of the Pt film along x and y axis of the sample. This procedure is required since the focus of the Pt and Fe evaporators fall at different positions of the sample. Of course, in order to grow and analyze a well-defined system it is necessary to find a region of the sample where the two evaporators produce deposits of homogenous thickness.

Pt $4f_{7/2}$ and Rh $3d_{5/2}$ core level spectra are shown in Fig. 4.7 and Fig. 4.8 at different y positions keeping x position fixed. The intensity of the Pt $4f_{7/2}$ core levels along the y axis is maximum at the position y=16mm and decreases slightly at y=15mm and y=17mm. A higher decrease of the Pt $4f_{7/2}$ core level intensity is observed at y=14mm and y=18mm. The trend of the intensity variation of the Rh *3d* core levels as a function of y variation (see Fig. 4.8) is in line with the corresponding Pt $4f_{7/2}$ core level spectra intensity variation (see Fig. 4.7). The lowest intensity is at y=16 mm while it slightly increases at y=15mm and y=17mm and is higher at the extreme sides y=14mm and y=18mm. We concluded that the Pt film thickness is homogeneous in the y range of 15mm<y<17mm. The homogeneity of the Pt deposit along the x axis can be estimated from the Pt $4f_{7/2}$ and Rh $3d_{5/2}$ core levels shown in Figures 4.9 and 4.10. Comparison of the spectra shows good coherency in the middle section (x=30mm, 31mm, 32mm) with very small deviation. The intensity decreases by moving towards the edge (x=33mm) and almost disappears on x=34mm.

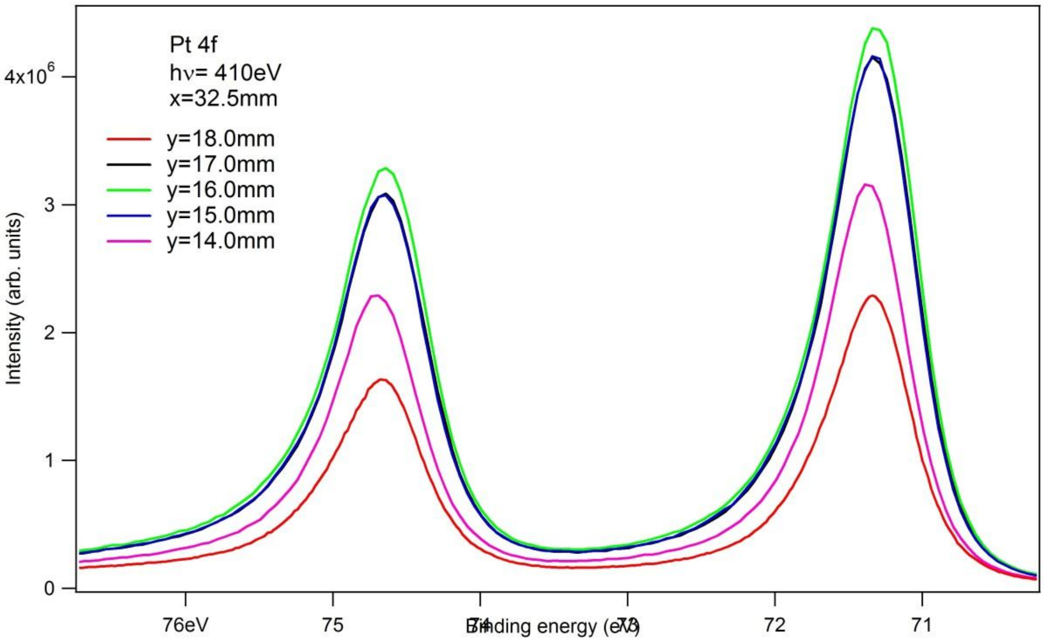

Figure 4.7 Pt 4f core levels spectra measured at different y position of the sample.

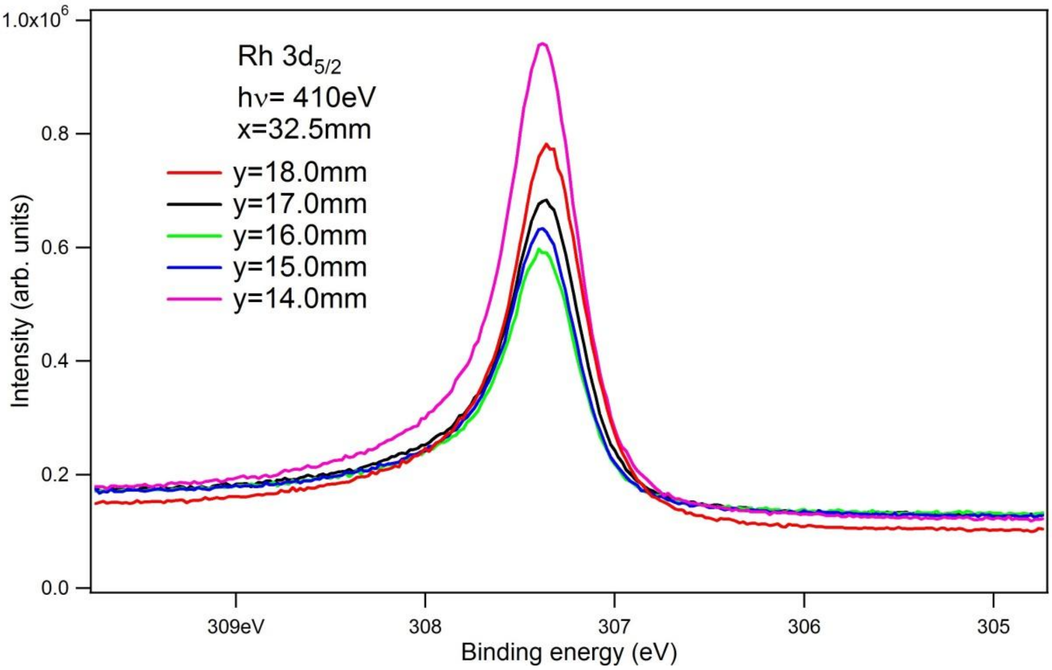

Figure 4.8 Rh 3d3/2 core level spectra measured at different y position of the sample.

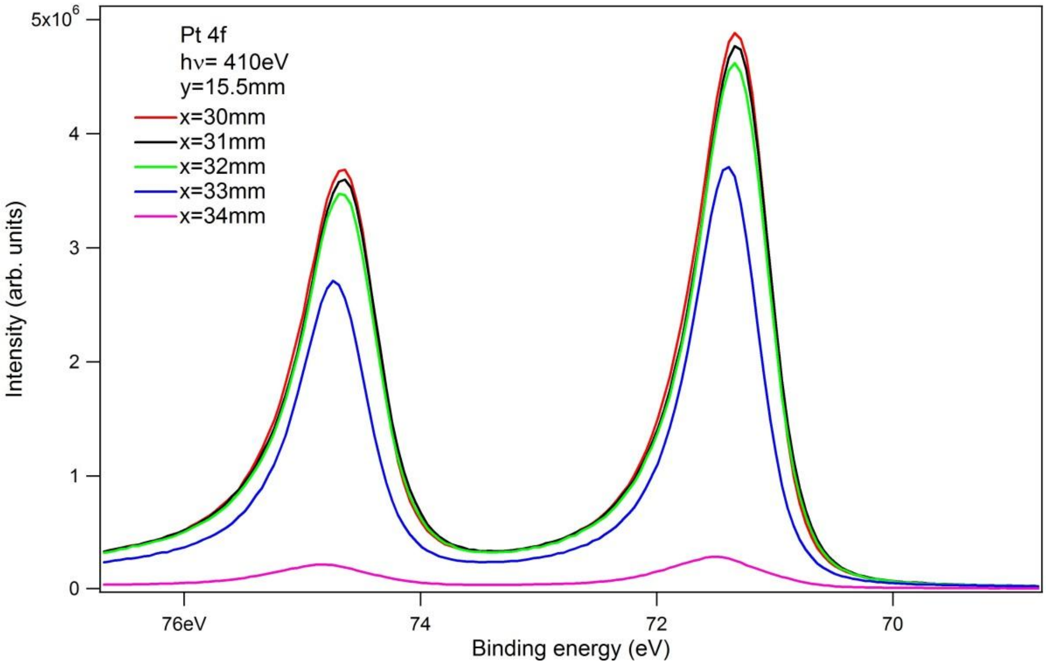

Figure 4.9 Pt 4f core level spectra measured at different x position of the sample.

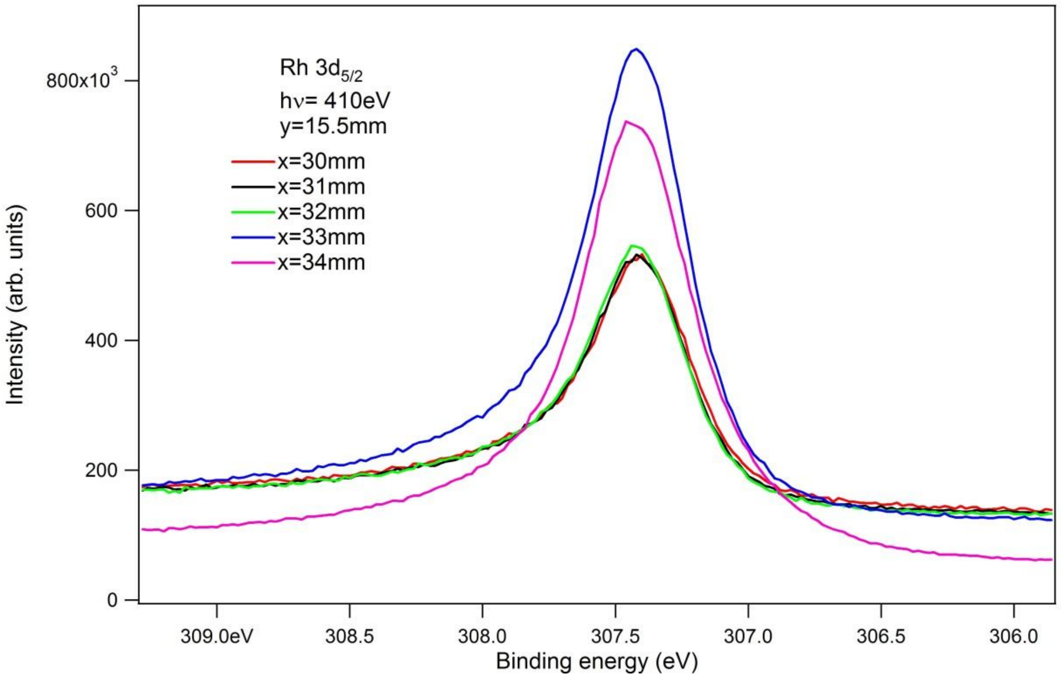

Figure 4.10 Rh 3$d_{5/2}$ core level spectra measured at different x position of the sample

For Fe we repeated the calibration procedure and checked the homogeneity of the film thickness for the different sample position. We performed this procedures after we prepared a new Rh (100) sample surface following the procedure described in Sec. 4.1.

The estimated evaporation rate was 2ML/min±0.5ML setting the Fe evaporator parameters at filament current 2.21A, voltage of the Fe rod at a +1KV with an emission current of 9.0 mA.

On the evaporated Fe film we measured the Fe 3*p* core levels shown in figure 4.11 for different x and y positions. By comparing the core level intensities we concluded that also for Fe, in the sample region 30mm<x<32mm and 15mm<y<17mm, the film thickness is homogenous with a maximum difference of less than 0.3 ML.

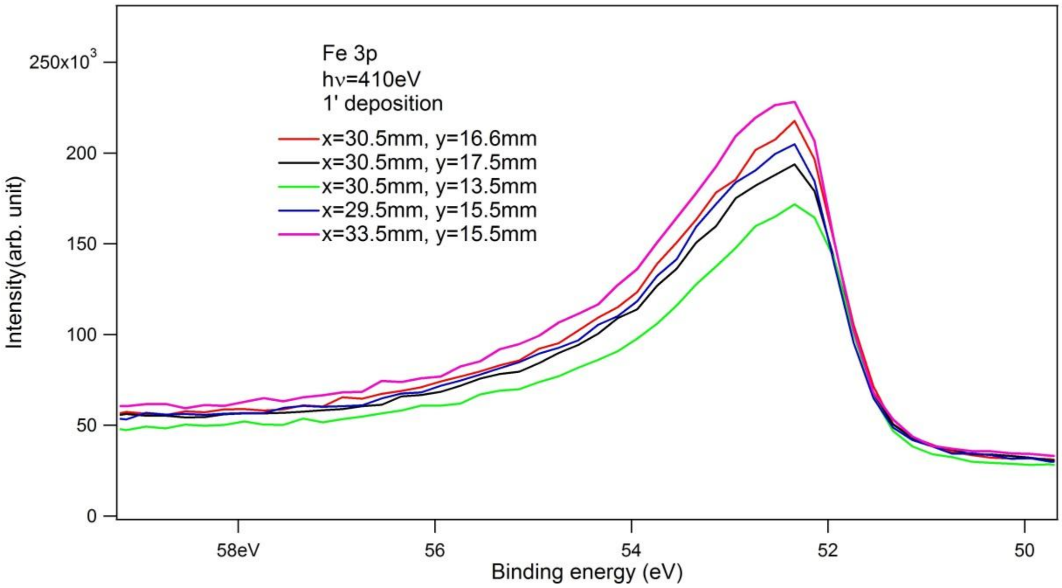

Figure 4.11 Fe 3*p* core level spectra measured at different sample positions.

4.3 XPS characterization of the FePt alloy grown on the Rh(100) surface

The FePt alloy was obtained by annealing at 380 °C 5 stacked bi-layers composed by 1 ML of Pt and 0.5 ML of Fe subsequently deposited on top of a thick buffer layer of Pt (13ML) + Fe (2ML) grown on clean Rh(100). The chemical composition and the surface atomic structure at the different growth steps were monitored by measuring the Pt 4$f_{7/2}$ (Fig.4.12) and Fe 3*p* core level spectra and the LEED pattern respectively.

The 13 ML film of Pt was deposited on top of the Rh(100) clean surface at room temperature (RT). After the Pt deposition we annealed at 380˚C and observed a well-defined 5x1 LEED pattern. It is known that Pt forms well-defined, large-scale *quasihexagonal* (“hex”) surface reconstructions [17]. The reconstructions imply a significant rearrangement of surface atoms and the creation of qualitatively distinct surface areas (steeper vs flatter ridges). The reconstructed Pt (100) surface exposes a quasihexagonal close-packed top layer with a 5x1 LEED pattern. These local structure variations in Pt (100) surfaces is the key ingredient for subsequent nanostructure growth and processes on top, e.g., by way of a preferential nucleation of deposits. For the 13ML thick Pt film, the Pt 4$f_{7/2}$ core level spectrum (Fig. 4.12 , black line) is a single peak centered at 71 eV binding energy (A).

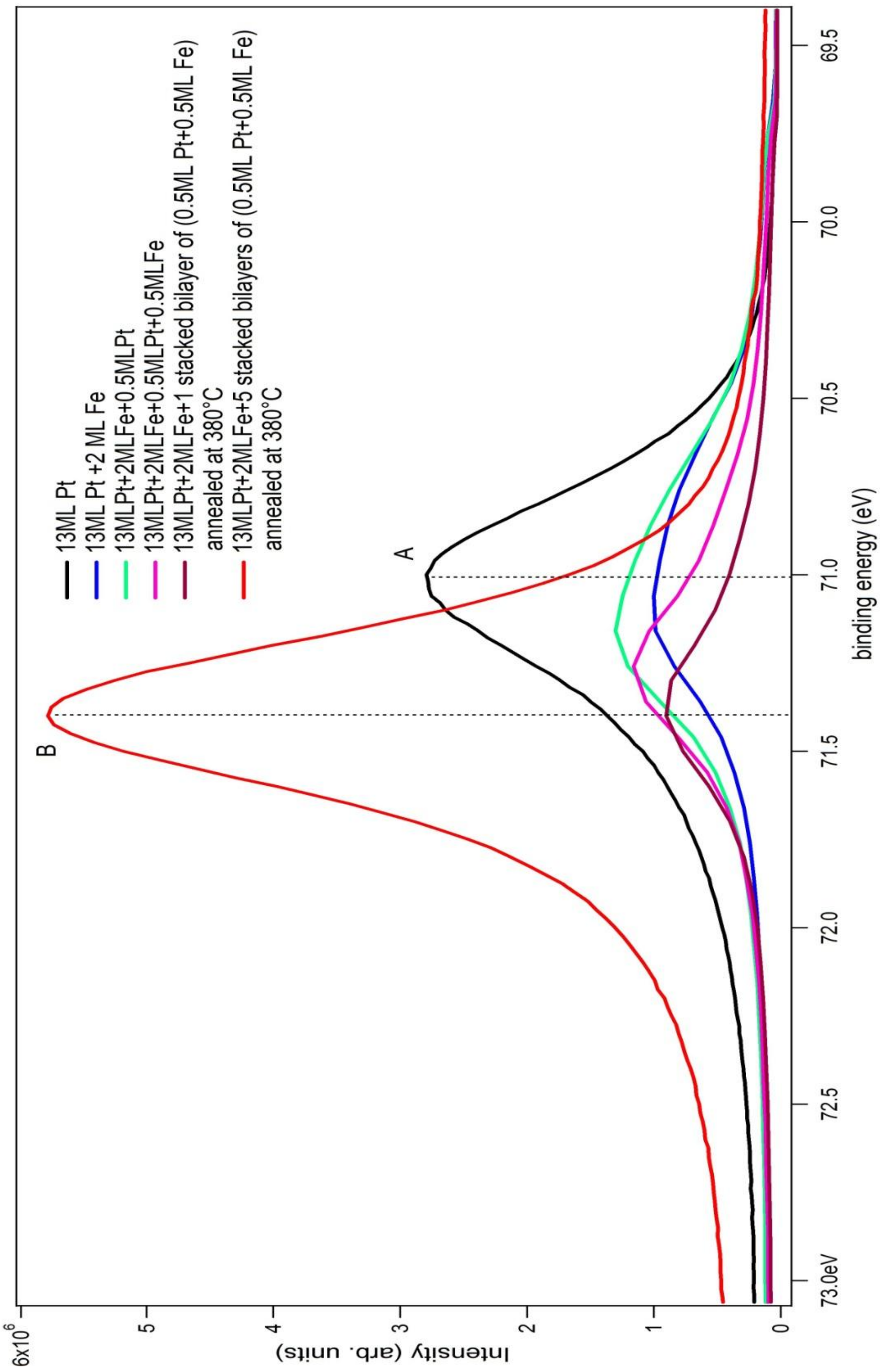

Figure 4.12 Pt 4f7/2 core level spectra measured at the different stage of the Fe-Pt multilayer growth. The A binding energy (71 eV) refers to the 4$f_{7/2}$ core level binding energy of metallic Pt while the B binding energy (71.39 eV) refers to the 4$f_{7/2}$ core level binding energy of Pt-Fe alloy formation [18]

We deposited 2ML of Fe on the surface of the thick Pt film at RT and observed a very good 1x1 LEED pattern. The Pt $4f_{7/2}$ spectrum (Fig.4.12 blue line) has a reduced intensity and different line shape. The photoemission peak is asymmetric, mainly composed by two energy shifted components. The spectral weight is transfer towards higher binding energy. Previous photoemission studies of Fe-Pt alloy formation [18] found that Pt atoms alloyed with Fe atoms give rise to a $4f_{7/2}$ core level peak shifted of about 0.4 eV higher binding energy with respect to the metallic Pt $4f_{7/2}$ core level peak. By depositing 0.5 ML of Pt (Fig.4.15 green line) the Fe-Pt peak intensity increases with respect to the metallic one. The deposition of 0.5 ML of Fe at RT onto top of the previous Pt layer induced an additional reduction of the Pt metallic component and an increase of the Fe-Pt component in the $4f_{7/2}$ core level spectrum (Fig.4.12 magenta line). The corresponding LEED pattern of this film coverage was a bad 1x1. In order to improve the crystalline quality of the film we annealed the sample at about 380 ˚C and we obtained a good 1x1 LEED pattern. After annealing the sample we observe a further increase of Pt-Fe alloy component present in the $4f_{7/2}$ core level spectrum with respect to the metallic one (Fig.4.12 brown line).

Based on the $4f_{7/2}$ core level spectra evolution as a function Fe/Pt layer stacking and annealing temperature we concluded that a good strategy for the Fe-Pt alloy preparation is to stack bilayers of 0.5ML of Fe and 0.5 ML of Pt deposited at room temperature and subsequent anneal the multilayer to 380 ˚C which clearly promote both crystalline order and alloy formation.

We deposited a total of 5 bilayers on top of the thick buffer layer and we observed a good 1x1 LEED pattern. The corresponding Pt $4f_{7/2}$ spectrum (Fig. 4.12 red line) is a single component core level (B) shifted by 0.39 eV to higher biding energy with respect to the metallic component (A) of Pt layer as deposited on Rh(100) surface.

4.4 Electronic properties of FePt alloy

The electronic properties of FePt alloy film were studied by measuring the valence band state dispersion by means of ARPES. The measurements were performed on the sample whose preparation and characterization were described in Sec. 4.3. Before ARPES measurements the sample was aligned in front of the LEED apparatus (see Fig. 4.13) and the band dispersion was investigated along the Γ-X direction.

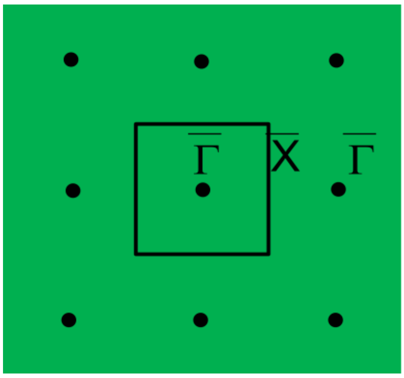

Figure 4.13 Schematic representation of the LEED pattern measured on FePt alloy film (black dots are LEED diffraction spots). The black square is the FePt unit cell with the high symmetry points. The sample was mounted in a way that the band dispersion was measured along the Γ– X direction

The intensity of the valence band structures depends on the energy of the exciting light. In Fig. 4.14 we report the photoemission intensity map of FePt alloy measured at different photon energies. We observe that depending on the photo energy the intensity of valence band states change. At photon energy of 70 eV, all the electronic structures are clearly visible. We select this photon energy to perform the following band structure investigations. The photoemission intensity maps shown in Fig.4.14 were acquired by setting the energy range [0 eV, -7 eV] from the Fermi level and the angular range [-15deg,+15deg].

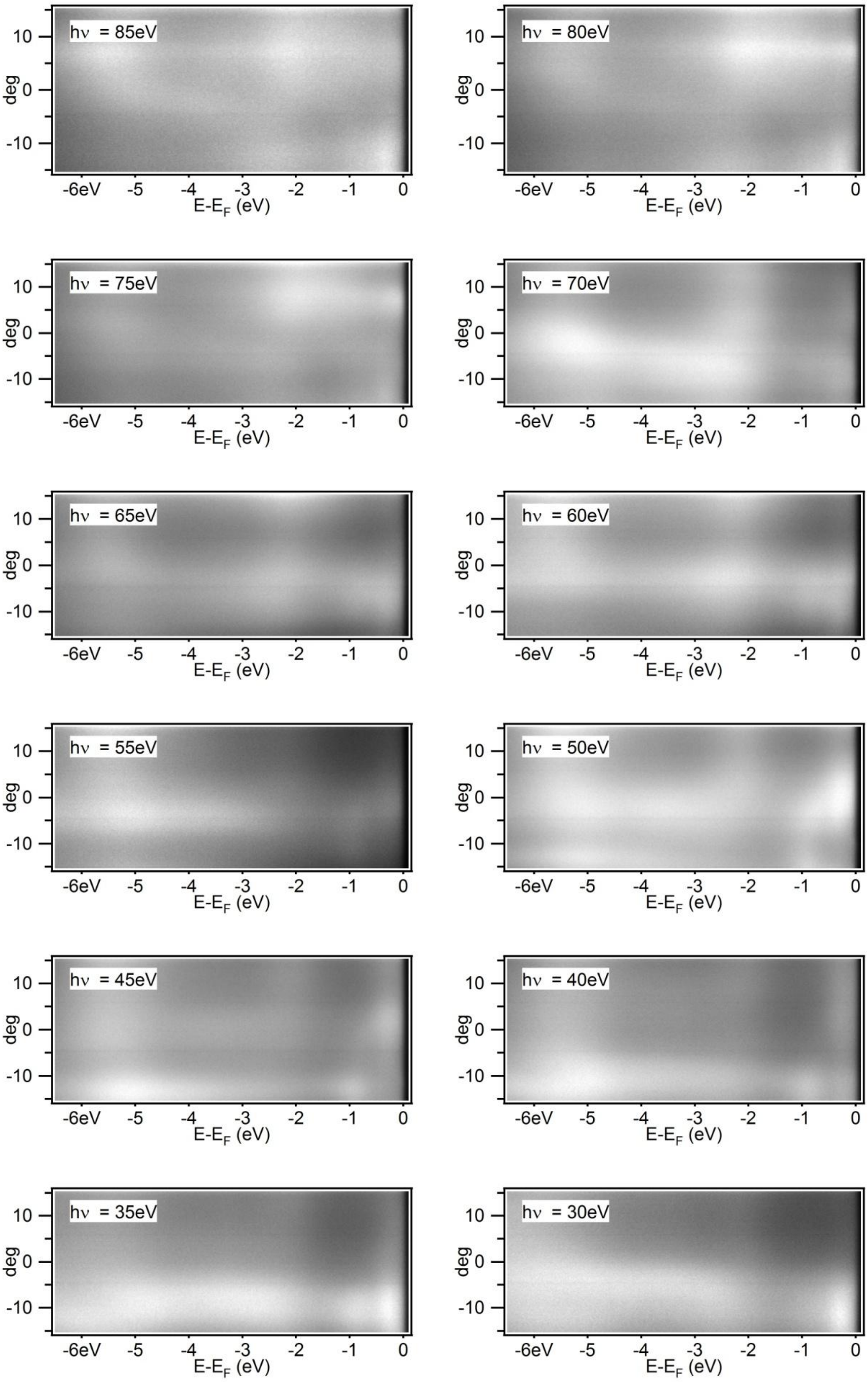

Figure 4.14 Photoemission intensity maps of FePt alloy measured at different photon energy.

In Fig.4.15 the photoemission intensity map of FePt alloy measured at 70eV photon energy is shown. The 2D matrix was acquired by setting the same energy and angular range of the previous set of measurements (Fig. 4.14), but longer acquisition time in order to improve the signal to noise ratio. The image reported in Fig. 4.15 is obtained from the original 2D data. The horizontal axis (emission angle axis) is converted to a$k_{||}$ momentum axis through the formula (3) (see also Sec. 3.4). The transformation from θ to $k_{||}$ was done by a macro written using the Igor Pro 6.12 software. The $k_{||}$ range is [-0.45 + 0.45] $Å^{-1}$.

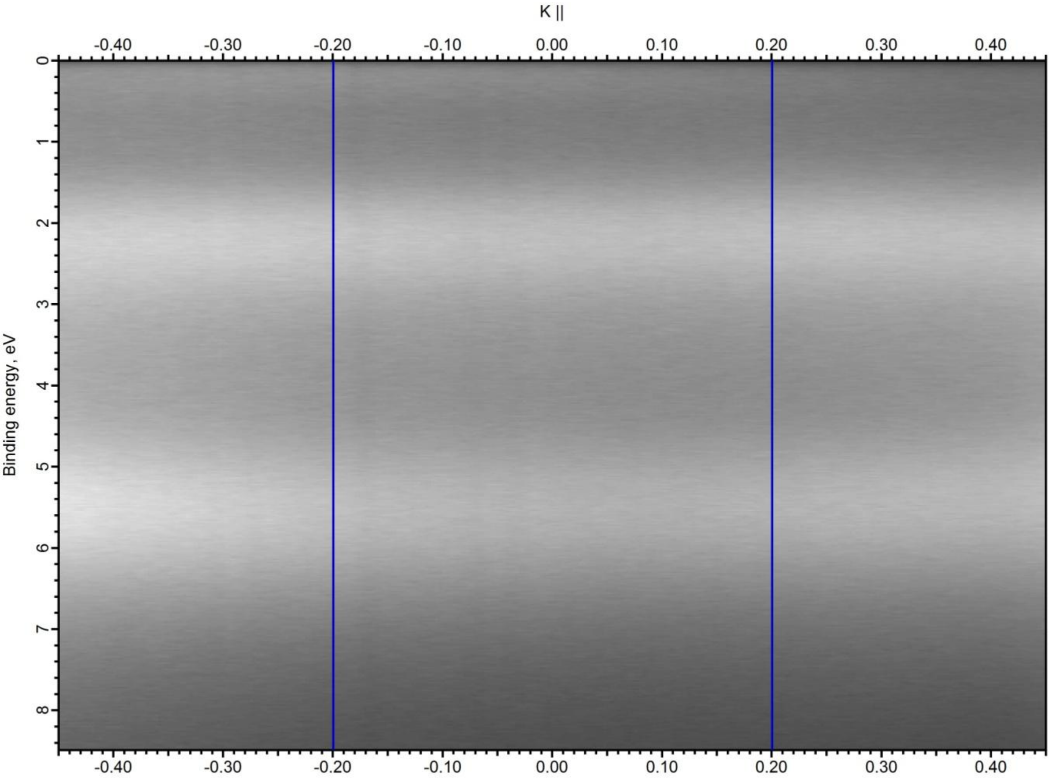

Figure 4.15 Photoemission intensity map of FePt alloy measured at 70eV

In the map we clearly distinguish two flat electronic bands at about 2eV and 5.5 eV from the Fermi level and a less intense structure at about 0.2 eV form the Fermi level. In Fig. 4.16 we report the valence band spectrum obtained by integrating the photoemission intensity map in the $k_{||}$ momentum range -0.2 $Å^{-1} < k_{||} < 0.2$ $Å^{-1}$. According to previous photoemission analysis [19] the state near the Fermi level (A) originate from Fe 3*d* levels, while the other two structures (B and C) derive from Pt 5*d* states. The relative intensity between the electronic structures in the valance band is the one already measured for the polycrystalline FePt alloy [19].

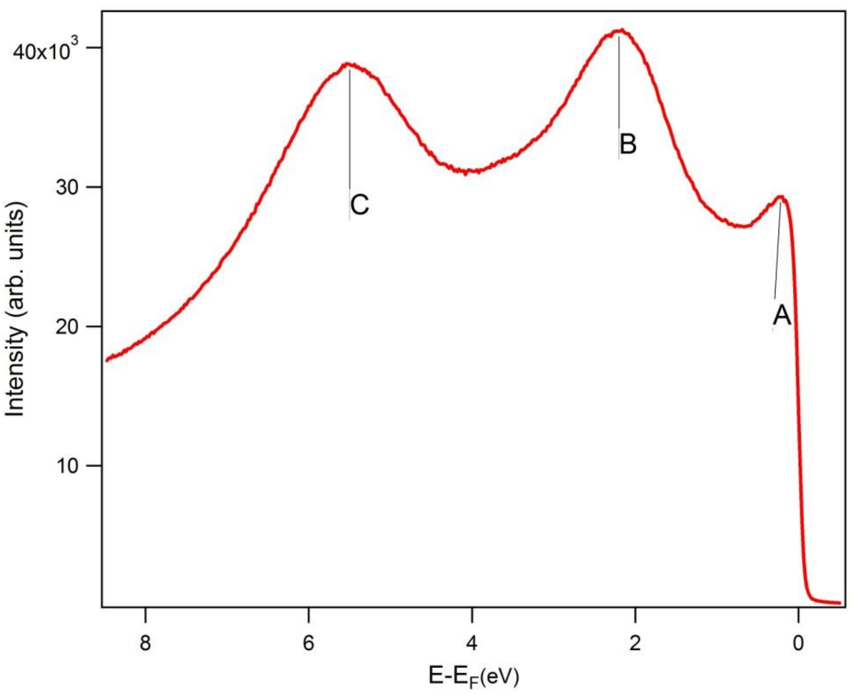

Figure 4.16 Valence band spectrum obtained from photoemission intensity map depicted in Fig. 4.15 by integrating the intensity signal in the range -0.2< k‖<0.2 Å-1. The structure A originate from Fe 3d levels, while the other two (B and C) derive from Pt 5d states. The spectrum is in agreement with the one already measured for the FePt alloy [19]

5. Conclusions

FePt film alloy was grown on Rh (100) surface by alternating deposition of Fe and Pt layers at room temperature with subsequent annealing at 380˚C.

XPS core level measurements combined with qualitative LEED analysis were used to characterized the preparation of the clean Rh (100) surface, the calibration of Fe and Pt evaporators and the alloy formation. For the evaporators calibration a simple attenuation model was used. The FePt alloy formation gives rise to a well resolved component in the $4f_{7/2}$ photoemission spectrum.

Photoemission intensity maps of the FePt alloy were measured and three main flat bands were identified. The integrated valance band spectrum is in agreement with previous photoemission analysis [19] performed on polycrystalline FePt alloy.

In conclusion, with the present work we find the conditions for the *in-situ* growth of FePt film on Rh (100). This preliminary study will serve for further ARPES investigation which will better describe the behaviors of the electronic bands that are responsible of the exceptional magnetic properties of FePt $L1_0$ alloy.

BIBLIOGRAPHY

[1] G.H.O. Daalderop, P.J. Kelly, and M.F.H. Schuurmans, Phys. Rev. B, **44**, 1254 (1991).

[2] R. F. C. Farrow, D. Weller, R. F. Marks, M. F. Toney, A. Cebollada, and G. R. Harp, J. Appl. Phys. **79**, 5967 (1996).

[3] B. M. Lairson, M. R. Visokay, R. Sinclair, and B. M. Clemens, Appl. Phys. Lett. **62**, 639 (1993).

[4] M. Doi, B. Roldan Cuenya, W. Keune, T. Schmitte, A. Nefedov, H. Zabel, D. Spoddig, R. Meckenstock and J. Pelzl, J. Magn. Magn. Mater. **240**, 504 (2002).

[5] Friedrich Reinert and Stefan Hüfner, New J. Phys. **7,** 97 (2005).

[6] John C. Vickerman, Ian S. Gilmore, 2009, *Surface Analysis – The Principal Techniques*, 1st edition, John Wiley & Sons Ltd, 47-110.

[7] Yeh J J and Lindau I, 1985 Subshell photoionization cross sections *At. Data Nucl. Data Tables* **32, 2 (**1985**)**.

[8] "Angle-Resolved Photoemission as a Tool for the Study of Surfaces," E. W. Plummer and W. Eberhardt, *Advances in Chemical Physics* **49**, ed. by I. Prigogine and S. A. Rice, John Wiley and Sons, New York, 1982, p. 533.

[9] C. N. Berglund and W. E. Spicer, Phys. Rev. A **136,** 1044 (1964).

[10] Hans Lüth, 1993, *Surfaces and interfaces of solids*, 2nd edition, Springer-Verlag Berlin.

[11] Philip Hofmann, lecture notes on surface science (20.6.2012)
http://www.philiphofmann.net/surflec3/index.html

[12] Philip Hofmann's ultra-high vacuum (UHV) pages (20.6.2012)
http://philiphofmann.net/ultrahighvacuum/home.html

[13] Sincrotrone Trieste (10.5.2012), http://www.elettra.trieste.it/

[14] Lightsources.org (16.7.2012) http://www.lightsources.org/imagebank/search_detail.php?image_no=SOL008

[15] Scienta hemispherical analyzer (10.7.2012) http://arpes.stanford.edu/images/SSRLAnalyzer.png

[16] Alessandro Baraldi, Giovanni Comelli, Silvano Lizzit, Renzo Rosei, Giorgio Paolucci, Phys. Rev. B **61**, 12 713 (1991).

[17] P. Heilmann, K. Heinz, K. Müller, **83**, 487 (1979).

[18] Dmitri I. Jerdev, Bruce E. Koel, Surf. Sci. **513,** L391 (2002).

[19] J. F. Van Acker, P.J. Weijs, J.C. Fuggle, K. Horn, H. Haak and K.H.J. Buschow, Phys. Rev. B, **43**, 8903 (1991).